UNITED STATES
DEPARTMENT OF THE INTERIOR
GEOLOGICAL SURVEY

INTERAGENCY REPORT: ASTROGEOLOGY 75

Correlation of photogeology and remote sensing data along the Apollo 14 Bistatic-Radar ground track, Part I—a working compendium

by

H.J. Moore, G.L. Tyler, J.M. Boyce, R.W. Shorthill, T.W. Thompson, A.S. Walker, D.E. Wilhelms, S.S.C. Wu, and S. H. Zisk

June, 1975

(Openfile Report 75-284)

Prepared by the Geological Survey for the National Aeronautics and Space Administration

Contents

List of Illustrations

List of Illustrations--Continued

List of Illustrations--Continued

List of Illustrations--Continued

List of Tables

Abstract

Photography and geology along the Apollo 14 Orbital bistatic-radar ground track have been compared with the surface roughness estimates determined by the Orbital radar at two frequencies (S-band and VHF). Visual estimates of roughness and topographic descriptions of geologic units correlate very well, but not perfectly, with the roughness estimates derived from bistatic-radar.

Terrestrial remote sensing observations, which include 3.8 cm and 70 cm backscattered diffuse component echoes and infrared eclipse temperatures, are correlated with the bistatic-radar ground track. Direct correlations of averaged values of the remote sensing measurements for selected geologic map units are found for: 1) root-mean-square (rms) slopes of the S-band and VHF radars, 2) 3.8 cm and 70 cm depolarized echoes, 3) S-band rms slopes and 3.8 cm depolarized echoes, 4) S-band rms slopes and 70 cm depolarized echoes, and 5) relative age of a surface and both S-band and VHF rms slopes. Inverse correlations of averaged measurements for selected geologic units are found for: 1) S-band rms slopes and infrared eclipse temperatures, and 2) VHF rms slopes and infrared eclipse temperatures.

Frequency distributions of bistatic-radar rms slopes, 3.8 and 70 cm depolarized echoes, and infrared eclipse temperatures for selected geologic map units are, in part, Gaussian, and in some cases may permit further subdivision of geologic map units.

The results of surface roughness determined by photogrammetric methods have marked parallels with those determined by the bistatic radar. Roughness characteristics of experimentally cratered surfaces show parallels with those of the Moon.

Particular emphasis has been placed on correlation of the various data sets in order to expose problems worthy of further study. The problems are listed at the end of the report.

I. Introduction

Apollo 14 was the third mission to land men on the surface of the Moon, the first to obtain photography of metric quality from orbit, and the first to perform the Apollo Orbital Bistatic Radar Experiment. The Apollo photography and Lunar Orbiter imagery combined with results from the bistatic-radar measurements, terrestrial remote sensing data, and photogeologic mapping provide an opportunity to intercompare the various results along the specular ground track of the bistatic-radar and interpret the results.

This report is a preliminary attempt to refine, intercompare, and interpret the available data. Some needed data sets are not yet available and others need to be calibrated; so that further intercomparisons remain to be done.

The ground track of the Apollo 14 Bistatic Radar Experiment (Howard and Tyler, 1971, 1972a) covers a thin strip across the near side of the Moon from a point southwest of Langrenus ($\approx 58^{\circ}$ E., 12° S.) to about 82° W. and 1° N. A wide variety of geologic map units were sampled.

In comparing results from the bistatic radar and terrestrial remote sensing data, average values of remote sensing measurements for various geologic units are used because actual areas for the given selenographic coordinates of the data sets may not correspond exactly.

II. Data sources and methods

A. Photographic data

Previous orbital photography.--Photographic coverage along the bistatic-radar ground track was obtained by Lunar Orbiter spacecraft (National Space Science Data Center, 1969). Nearly complete coverage of the lunar near-side at a resolution of about 30 m was obtained by Lunar Orbiter IV. Additional photographic coverage of local areas on or near the bistatic-radar track was obtained by Lunar Orbiters I, II, III, and V with resolutions down to 1.0 m. For this study, photographs from the Lunar Orbiters were used in comparing visual impressions of surface roughness with bistatic-radar results, in estimating regolith thicknesses, and in determining relative ages of surfaces.

Apollo 14 photography.--A variety of orbital photographic coverage was

obtained by Apollo 14 along and near the bistatic-radar ground track (National Space Science Data Center, 1971a, b, c; Aeronautical Chart and Information Center, 1971). Photography from the Lunar Topographic Camera is of special interest here because its metric quality combined with stereoscopic coverage permits the extraction of quantitative information regarding lunar surface roughness. This camera obtained photographs with a surface resolution near 2.0 m and was calibrated for focal length and lens distortions. Stereoscopic coverage permits the use of standard photogrammetric techniques. Other Apollo 14 photography was not used.

Subsequent photography.--Apollos 15, 16, and 17 obtained photography along the eastern part of the Apollo 14 bistatic-radar track. Only Apollo 16 obtained significant coverage of the Apollo 14 track with both the Metric and Panoramic Cameras (Defense Mapping Agency, Aerospace Center, 1972). Post-Apollo 14 photography and results are used to a limited extent in this report for areal comparison of terrestrial remote sensing data sets and determining relative ages of surfaces.

B. Geology and geologic map units

Telescopic observations, spacecraft images, and photography show that reflectivity and topography of lunar surfaces are heterogeneous. In photogeologic mapping, surfaces are classified on the basis of topography, geometric distribution of topography, and albedo or reflectivity under full Moon illumination (see for examples, Shoemaker and Hackman, 1962, p. 289-300; Wilhelms, 1970, 1972). The topographic and optical properties of the surface are assumed to be an expression of underlying materials, so that surface units correspond to underlying rock units, which are analogous to the rock-stratigraphic units of terrestrial geology. The rock units are arranged in order of relative age and grouped into time-stratigraphic units by applying the concepts of superposition, intersection, and by apparent modification of their properties with time. Following terrestrial convention, the major time-stratigraphic units are designated systems; the systems recognized to date are Copernican, Eratosthenian, Imbrian (Wilhelms, 1970), and Nectarian (Stuart-Alexander and Wilhelms, 1975). Units older than Nectarian are not formally divided and are simply designated as pre-Nectarian. The Nectarian time-stratigraphic unit was defined recently and does not appear in the geologic maps or units in this report, so units older than Imbrian are designated pre-Imbrian.

Evidence collected by unmanned and manned missions has shown that the lunar

surface is significantly modified and altered on a fine-scale by impact cratering (Shoemaker and others, 1969; Soderblom, 1970; Moore, 1964, 1971a; and Moore and others, 1974). One of the end results of this impact cratering is the production of a fragmental layer (regolith) with remarkably uniform mechanical properties but with variable thickness (Shoemaker and others, 1969). Because the thickness of the regolith layer varies from place to place, unmodified materials of the stratigraphic units mapped may not occur at the surface but at a depth that depends on the degree of modification, local slopes, and recent exhuming events such as impact cratering (Shoemaker, 1960; Moore, 1971b). The thickness of the regolith is usually greater than a few meters but can vary from a few centimeters to tens of meters and more. The physical, mechanical, and electrical properties of the uppermost fragmental layer (regolith) do not vary widely from place to place (see for examples, Howard and Tyler, 1972b, p. 25(12)-25(13); Costes, 1973). In spite of the impact crater modification, geologic mapping (Wilhelms, 1970) and results from the orbital X-ray Fluorescence Experiment (Adler and others, 1972a, b) demonstrate that topographies, albedos, and chemical compositions of the underlying units have not been entirely obliterated.

Many of the geologic maps used below were prepared using Earth-based telescopes without the benefit of spacecraft images, photography, or other remote sensing data. Incorporation of these additional data will require modification of distributions and stratigraphic relationships of the earlier geologic map units and may provide new map units.

Eight geologic maps at 1:1,000,000-scale are traversed by the bistatic-radar ground track between 70° E. and 70° W.: (1) Langrenus--LAC 80[1/] (Hodges, 1973), (2) Colombo--LAC 79 (Elston, 1972), (3) Theophilus--LAC 78 (Milton, 1968), (4) Ptolemaeus--LAC 77 (Howard and Masursky, 1968), (5) Riphaeus Mountains--LAC 76 (Eggleton, 1965), (6) Copernicus--LAC 58 (Schmitt, Trask, and Shoemaker, 1967), (7) Kepler--LAC 57 (Hackman, 1962), and (8) Hevelius--LAC 56 (McCauley, 1967). Geologic map units sampled by the bistatic-radar are chiefly mare materials, crater materials

---

1/ LAC 80 refers to Lunar Aeronautical Chart 80 which is one of a series of shaded relief maps published by the Aeronautical Chart and Information Center (U.S. Air Force, St. Louis, Missouri 63118) at 1:1,000,000-scale.

of various ages, and a variety of upland units. Units sampled and their characteristics are summarized in Table 1 where Langrenus (LAC 80) and Copernicus (LAC 58) quadrangles have been omitted. For Langrenus, bistatic-radar results are incomplete; for Copernicus, only a small part was sampled. Units from the Riphaeus Mountains region (LAC 76) are the same as the units in the Copernicus quadrangle (LAC 58). Designations for some units have been modified for this report as a result of new data. These modifications are indicated in Table 1.

Mare materials, unit Im (formerly symbolized Pm and Ipm), have extensive, relatively smooth horizontal surfaces that terminate abruptly against many topographic forms. Widely separated ridges stretch across mare surfaces in sinuous en-echelon, and linear patterns. The ridges may be broad and low or narrow and steep; and commonly, the two types are superposed. These ridges are mapped as mare materials. The albedo of mare materials is generally low with small lateral variation. Some mare materials have very low albedos (< 0.06 percent) and are designated Imd[1/] (formerly Ipmd). For these dark mare materials, topographic expression is similar to other mare surfaces, but the density of craters greater than about 1 km across is less than other lighter maria (McCauley, 1967). In the present report area, dark mare materials are found chiefly in the Hevelius quadrangle--LAC 56 (McCauley, 1967). The Cavalerius Formation (Cca), which has no intrinsic relief and low albedo (McCauley, 1967) where sampled by the bistatic-radar, is included with mare materials.

Crater units sampled by the bistatic-radar, in approximate order of relative age, are: Copernican, Eratosthenian, Eratosthenian-Imbrian, and Imbrian. In a broad sense, the topography of these craters and their sub-units are similar. However, they differ in albedo and degree of preservation of the topographic expression of the sub-units. Copernican craters appear fresh, topographies of sub-units show the greatest relief, rays and secondary craters extend to great distances, and their albedos have high contrast--mostly higher than the surroundings. Eratosthenian craters also appear fresh with well preserved topographic details, but their

---

1/ The unit symbolized Imd in the Colombo quadrangle--LAC 79 (Elston, 1972)--represents mare domes and not mare material. The Colombo domes were not sampled by the bistatic-radar.

Table 1. Geologic map units sampled along Apollo 14 bistatic-radar sub-specular ground track.

Geologic Units	Designator	LAC 56	chart 57	numbers of 58-76	quadrangle in which units are mapped 77	78	79	Characteristics
Mare units								
Dark mare material	Imd[1]	x						Materials of dark smooth horizontal surfaces; fewer superposed craters and rays than Im
Mare material	Im[2]	x	x	x	x		x	Smooth horizontal surfaces with widely separated ridges
Crater units								
Copernican								Materials of rayed craters with well preserved topographic detail
Central Peak material	Ccp							Irregular central hill rising above crater floor (not sampled)
Floor material	Ccf				x			Level, partly hummocky in larger craters
Wall material	Ccw(Cs)				x	x		Steep slopes, hummocky to smooth
Hummocky rim material	Ccrh					x		Hummocky
Steep rim material	Ccrs				x			Steep, hummocky rim
Radial rim material	Ccrr					x	x	Radial ridges
Rim material	Ccr		x	x	x	x	x	Hummocky surfaces and radial ridges around larger craters
Rim material	Cr		x					Hummocky surfaces and radial ridges around smaller craters
Theophilus Fm., smooth	Cts					x		Smooth level surface
Theophilus Fm., hummocky	Cth					x		Hummocky, topography similar to Ccrh
Eratosthenian								Materials of non-rayed craters with well preserved topographic detail
Central peak material	Ecp							Steep hills near crater centers (not sampled)
Floor material	Ecf							Smooth to slightly hummocky (not sampled)
Wall material	Ecw(Cs)		x				x	Steep slopes
Radial rim material	Ecrr	x						Subdued radial ridges
Hummocky rim material	Ecrh							Hummocky (not sampled)
Rim material	Ecr	x	x				x	Hummocky with radial ridges
Crater material	Ec						x	Small craters
Eratosthenian-Imbrian								Materials of non-rayed craters with preserved topographic detail
Central peak materials	EIcp				x			Irregular central hill rising above crater floor
Floor materials	EIcf				x			Level partly hummocky
Crater wall materials	EIcw				x			Steep slopes, hummocky to smooth
Grid pattern rim materials	EIrg				x			Lineated
Crater rim materials	EIcr				x			Hummocky to rolling, radial ridges
Imbrian								Materials of non-rayed craters with subdued topographic detail
Central peak materials	Icp			x				Rugged hills
Floor materials	Icf			x				Smooth to gently rolling
Crater wall materials	Icw			x				
Crater rim materials	Icr	x		x				Hummocky around craters wider than 15 km
pre-Imbrian								Materials of non-rayed craters with obliterated topographic detail
Crater wall materials	pIcw						x	Steep slope, hummocky, terraced or smooth
Crater rim materials	pIcr						x	Hummocky to faintly hummocky
Crater materials	pIc				x		x	Craters

(Continued)

Table 1--Continued. Geologic map units sampled along Apollo 14 bistatic-radar sub-specular ground track

Geologic Units	Designator	LAC 56	chart 57	numbers 58-76	of 77	quadrangles 78	in 79	which units are mapped Characteristics
Imbrian upland units								
Plains material	Ip						x	Level smooth light plains
Cayley Formation, smooth	Icas					x		Level smooth light plains
Cayley Formation, hummocky	Icah					x		Low hills
Cayley Formation	Ica				x			Like Ip, or Icas and Icah undivided
Smooth material	Is				x			Smooth rolling surface with rounded hills and craters
Terra material	It				x			Smoothed, hilly upland
Regional material	Ir[3]		x					Hummocky, hilly and pitted
Fra Mauro Formation	If			x				Hummocky, commonly with linear hummocks
Fra Mauro Fm., hummocky	Ifh				x			Hummocky
Irregular material	Ii						x	Hilly and furrowed
Subdued hummocky material	IpIh						x	Hilly to hummocky, subdued
Hummocky material	Ih						x	Hilly to hummocky
Materials of Kant plateau, smooth	Iks					x		Raised, broadly rolling smooth surface
Materials of Kant plateau, pitted	Ikp					x		Broadly rolling and pitted
Materials of Kant plateau, rugged	Ikr					x		Rugged-twisting elongate depressions and hills
pre-Imbrian upland units								
Rugged terra of crater rims	pItc[3]					x		Rugged and furrowed terra of crater rims
Undivided	pIu[3]				x			Rugged terra
Rugged terra	pIt[3]					x	x	Rugged terra
Furrowed terra	pItf[3]					x		Furrowed terra

1/ Formerly Ipmd, 2/ Formerly Pm and Ipm, 3/ Itc, It, and Itf, on LAC 78

rays are virtually absent and have albedos that are more like the background than Copernican craters. The topography of the other older craters appears more subdued than the younger Copernican and Eratosthenian craters. All of the crater materials may have common sub-units regardless of age, while some sub-units are unique. Many of the craters have central peak materials (Ccp, Ecp, EIcp, and Icp) forming irregular steep hills that rise above the crater floor. Crater floor materials (Ccf, Ecf, EIcf, and Icf) are relatively level surfaces ranging from rugged and hummocky (Ccf) to smooth and gently rolling (Icf). Crater wall materials (Ccw, Ecw, EIcw, Icw, and pIcw) slope steeply inward toward the crater center and may be terraced. The flanks of craters are generally hummocky (Cr, Ccr, Ccrs, Ccrh, Ecr, Ecrh, EIcr, Icr, pIcr) and ridged (Cr, Ccrr, Ecrr, Ecr, EIcr). Locally, small smooth marelike patches (Cts) may be present.

Upland units include a host of terrain types such as terra plains, hummocky plains, undulating surfaces, rugged-grooved surfaces, rugged surfaces of crater rims, and rugged cratered surfaces. Terra plains may be smooth and marelike while others are more cratered than maria (Ip, Icas, Ica). Still other units are chiefly undulating (Is, It, Ica, Icah), or hilly (Ir, If, Ifh, Ii, IpIh, Ih). Hills, hummocks, craters, and depressions in these units are characteristically 0.5 to 4 km across. Surfaces, rugged at a coarser scale, include plateaus with hills, ridges, depressions 4-10 km across (Iks, Ikp, Ikr, pItc, pIr, pIt, pItf), and craters (pIcw, pIcf, pIcr, pIw).

In summary, the surfaces of mare materials (unit Im) are the smoothest at 1 km resolution--particularly those of the dark mare materials in Hevelius--LAC 56 (unit Imd or Ipmd; McCauley, 1967). Local areas in the uplands and around craters appear smooth and marelike (unit Ip; Elston, 1972 and units Icas, Cts; Milton, 1968). Other upland plains are more cratered (units Ica, Icas; Milton, 1968). Even the most rugged uplands have a few smooth patches, but most are too small to map at 1:1,000,000-scale.

Crater units are visually rough irrespective of their age--particularly those units near the crater rims and within the craters. Although Copernican and Eratosthenian craters have well preserved detail, the roughness of Eratosthenian-Imbrian and Imbrian craters measured in resolution cells of 6-20 km could equal that of the younger craters. Roughness for 6-20 km resolution cells also depends

markedly on sample location.

Upland plains--with the exception of smooth upland plains (Icas, Ip)--are visually rough because of their dense crater populations and their hilly to hummocky character. Some uplands may be very rough because of numerous large undulations, grooves, crater rims, and furrows.

C. Bistatic-radar

The radar data discussed here were obtained from the Stanford-Apollo Bistatic-Radar Investigation on Apollo 14 (Howard and Tyler, 1971). Theory and some of the results have been discussed elsewhere (Howard and Tyler, 1971, 1972a, 1972b). Radio frequency transmissions from the orbiting Command Service Module were received on Earth after reflection from the lunar surface. Two wavelengths were used simultaneously--13 cm and 116 cm (2287.5 Mhz and 259.7 Mhz). Because scattering from the lunar surface is dependent upon wavelength, the data provide a sampling of lunar surface properties at two different scales. At the present time, this wavelength dependence is understood only in a general way, although the longer wavelength measurements sample a larger scale length of surface features than the shorter wavelength.

The echo spectrum is broadened according to the probability-density function of the surface slopes expressed through the doppler shift. Complete lunar slope frequency distributions may be inferred directly from the bistatic-radar data (Parker and Tyler, 1973) although this has not been done here. Rather, single measures of roughness have been estimated from echo broadening. Here two estimates of surface roughness are reported for each wavelength. The first is called machine calculated root-mean-square (rms) slope and is obtained from the equivalent area bandwidths (Tyler and Howard, 1973) based on objective calculation of peak power spectral density and total signal power. The second is called hand calculated rms slope and is obtained by graphically measuring the bandwidth at the 1/2 power points of the echo spectrum (Tyler, Howard, and Dow, 1973). The root-mean-square slope is roughly equivalent to the algebraic standard deviation of a slope frequency distribution with an algebraic mean of zero.

The data correspond to averages over resolution cells varying from about 10 to 20 km in diameter. The best estimates of the horizontal surface scales corresponding to the slope measurements are about 30 m for S-band and 275 m for

VHF. However, the scale length resolution is not precisely known. This will be discussed later.

D. Terrestrial radar observations

The Earth-based radar observations used here were carried out at a wavelength of 3.8 cm from MIT Haystack Observatory (Zisk and others, 1974; Pettengill and others, 1974) and 70 cm from the Arecibo Observatory (Thompson, 1968, 1974). The experimental techniques are essentially the same although these observatories are quite different in their construction and engineering details. Circularly polarized signals were transmitted from the Earth, reflected from the lunar surface, and the echoes received on Earth. Upon reception, the returned signal was analyzed for two circular components: 1) circularly polarized in the sense expected from a smooth reflecting sphere, called the polarized component, and 2) circularly polarized in the opposite sense to that expected from a smooth reflecing sphere - called the depolarized component. Simultaneous resolution of the echo signal in time delay and doppler frequency is employed to generate area resolution cells on the order of a few kilometers on the lunar surface and to permit the scattering areas to be related to selenographic coordinates.

In general, radar experimenters have interpreted the depolarized echo as arising only from smaller, more randomly oriented structures, such as rocks or boulders, and the polarized echo as arising from a combination of the same small structures plus another component from large scale (> 10 wavelengths) surface undulations properly oriented to produce mirrorlike reflections toward the observer. The scale length of sensitivity of depolarized echoes is generally given as being on the order of a wavelength. While it is known that these relationships cannot be strictly true, particular attention has been given to the depolarized echoes because those echoes do provide a clear indication of relative surface roughness in some sense. A local enhancement in depolarized echoes is associated with one of the following factors:

1) An increase in the number of blocks in the upper ten wavelengths (approximately) of the lunar regolith (Thompson and others, 1974).
2) An increase in the relative dielectric constant of a normally rough or blocky surface.
3) A change in slope so that the surface is tilted toward the radar site.

4) Possibly, a decrease in the electromagnetic absorption in the upper part of the lunar regolith (Schaber and others, 1974; Pollack and Whitehill, 1972).

For the 3.8 cm data, radar echoes are collected in sets from relatively large areas of the Moon called ZAC charts (Zisk and others, 1974). Because the scale factors among the ZAC charts are not exactly the same, and the bistatic-radar track crossed several of these areas, a calibration procedure was required to match data sets at the ZAC chart boundaries. This was accomplished by assuming that the geologic unit on one side of an offset should have the same echo strength value as the same geologic unit on the other side of the offset. For the 3.8 cm data, echo strengths reported here are in the form of

$$E_{3.8} = \log_{10} P/P_e + \text{constant}$$

where P is the echo power and P_e is the expected behavior of the Moon at that angle of incidence. The echoes selected have the same selenographic coordinates as those for the bistatic-radar specular track. Resolution cells were originally 2 km across for the areas discussed here. These resolution cells were then summed into cells about 14 km across, to match the resolution of the other data sets.

For the 70 cm data, the echo strengths are scaled by 120 or

$$E_{70} = 120 \log_{10} P/P_A + \text{constant}$$

where P_A is the average background power received for a given LAC area. Again, the echoes selected have the same selenographic coordinates as the bistatic-radar specular track. Area resolution cells on the order of 5 to 10 km across were achieved and used without further averaging.

E. Infrared eclipse temperatures

The thermophysical properties of the lunar surface are studied by measuring the thermal emission from the Moon at infrared wavelengths. Ground based measurements are limited mainly to wavelength bands of 8 to 14 and 17 to 24 μm because of atmospheric absorption. Most measurements have been made in particularly narrow bands within the 8 to 14 μm window.

The thermal response of the lunar surface can be measured easily from the Earth during an eclipse when the average surface cools from the full Moon temper-

ature of about 400°K to about 150°K. The eclipse measurements have been reviewed by Shorthill (1970, 1972). The Moon was scanned in a rectangular raster during the penumbral phase of the lunar eclipse of December 19, 1964. A resolution of 10 arc seconds was achieved, corresponding to roughly 17 km at the subterrestrial point. Selenographic positions of the scans were determined by associating small lunar features with observed anomalies. Positions of eclipse temperatures were then correlated with selenographic positions corresponding to those of the Apollo 14 bistatic-radar specular ground track.

In order to compare different areas of the Moon on an equal basis, these data were normalized to the average behavior of the terrae (Shorthill and others, 1970; Shorthill, 1973). This procedure corrected for the decrease in temperature toward the limbs caused by the initial full Moon temperature distribution and the asymmetry in the cooling time caused by the passage of the Earth's shadow across the disk. This normalization produced a "flattened Moon" quantity, ΔFM, given by:

$$\Delta FM = \frac{(T_{observed} - T_{base})}{T_{full\ Moon}}$$

where $T_{observed}$ is the observed eclipse temperature, T_{base} is the expected localized background temperature, and $T_{full\ Moon}$ is the localized full Moon temperature. Scaled values used in this paper are:

$$IR = 100 + 1000\ \Delta FM$$

Localized high anomalies (hot spots) are believed to result from an excess of bare rocks on the lunar surface. Theoretical considerations support this (Roelof, 1968; Winter, 1970; Allen, 1971). These surface rocks must be about 10 cm or more in diameter, and the number of rocks per unit area must be larger than that observed by Surveyor 1 and 3.

F. Relative ages

Relative ages of cratered lunar planar units were obtained using the crater morphology technique described by Soderblom and Lebofsky (1972). In this method, an orbital photograph is examined to determine the largest diameter of clearly unshadowed craters in an area and the smallest diameter at which all craters are shadowed. These two diameters set the lower and upper limits, respectively, for the largest crater whose interior slope has been eroded to the solar illumination

angle. This diameter is termed D_s. D_s is then converted to D_L, the size of crater that is worn to a 1 degree interior slope using the small impact erosion model developed by Soderblom (1970). D_L values may, in turn, be related to absolute age using flux curves calibrated with radiometric dates from Apollo samples (Soderblom and Boyce, 1972).

The technique has been applied to all available lunar orbital photographs (Boyce and others, 1974). Here we will be concerned with data only along or near the Apollo 14 bistatic-radar ground track. Unfortunately, data along this track are scanty and available only from a few Lunar Orbiter images and Apollo 16 metric photographs.

G. Regolith thickness

Regolith thicknesses were estimated from Lunar Orbiter photography using a crater morphology technique developed on the basis of experimental impact data in the laboratory (Quaide and Oberbeck, 1968, 1969; Oberbeck and Quaide, 1967, 1968). In the experiments, normal craters with depth to diameter ratios near 1:4.4 were obtained for targets of homogeneous cohesionless sand. The presence of an indurated substrate overlain by cohesionless sand resulted in craters with central mounds, flat floors, and concentric structures when the sand thickness was sufficiently thin. The type of crater was then related experimentally to the thickness of the sand layer over the substrate. In applying the experimental results to the lunar surface, craters in individual size intervals are classified by form, and their relative abundance within each size interval was determined. From these data a probability distribution of regolith thickness is derived.

The procedures used here were modified to reduce the number of craters that must be counted. The 90 percent confidence interval for a thickness determined for a given size range of craters does not change after about 150 craters have been classified (Oberbeck, oral comm., 1974). Thus, a suitable sampling of small craters in an area that includes more than 150 craters within a given size range may be used to reduce the number of craters that are classified. This was accomplished by placing a grid over the photography and using a random number table to select areas in the grid to count and classify about 200 craters in the smallest

diameter intervals[1]. All craters with large diameters were counted. A comparison of results obtained with this sampling technique, and one using all craters showed that they were equivalent. On Apollo panoramic photographs all fresh craters were counted because of limited areal coverage.

Test results reported here for the Hadley rille area using Lunar Orbiter photography were in substantial agreement with the results of Oberbeck (unpub. data).

H. Photogrammetry

Photogrammetric data were obtained using stereoscopic pairs of Lunar Topographic Camera positive transparencies[2] on an analytical stereoplotter. Stereomodels were leveled and scaled using Lunar Orbiter imagery and data[3]. At least three elevation measurements were averaged for each point in the stereo-model and the points were separated by a horizontal fixed interval. This fixed horizontal interval is referred to below as slope length, Δ_L. Slopes are calculated from these data. About 450 or more elevations were determined for each slope-frequency distribution along a linear traverse so that the slopes are unidirectional. Slope-frequency distributions with slope lengths near 25 m and less are corrected for reading errors as outlined by Moore and Wu (1973). Slope-frequency distributions for larger slope lengths do not require this correction. They were derived from the photogrammetric elevation data using the U.S. Geological Survey's terrain analysis program[4].

III. Correlations and Comparisons

A. Comparison of bistatic-radar results with images

Relative surface roughness estimated visually on Lunar Orbiter IV high resolution images compares well with roughness or rms slopes obtained from the

---

1/ This procedure was suggested by E.B. Newman (Moore, Lugn, and Newman, 1974).

2/ The Lunar Topographic Camera (Hycon) has an optical resolution of 88 line pairs/mm. SO-349 type high-definition aerial film provided a ground resolution of 2.7 m. Lens distortions are less than 20 μm within 2.5 inches of the center of the 5 inch format. The calibrated focal length is 455.677 mm.

3/ Stereomodels were oriented using control points obtained from Lunar Orbiter imagery because of the unavailability of ground control points at the time of model setup.

4/ This program was written by Richard Godson, Gary Selner, Wesley Rozema, Dennis McMacken, and Stephen Wilson under the general supervision of R.J. Pike.

bistatic-radar observations. Details are shown in figures 1 through 13, which show the location of the bistatic-radar ground track on Lunar Orbiter IV mosaics and geologic maps (originally 1:1,000,000-scale). Below the mosaics and maps, hand calculated S-band and VHF rms slopes are plotted as a function of longitude. It is clear that surfaces that appear smooth in the photographs also appear smooth to the radar. Conversely, rough features such as craters are also rough to the radar. Detailed comparisons for each section are described below.

LAC 56 west (fig. 1). Although both rough upland and smooth mare terrains occur here, only the smooth appearing mare was sampled by the radar and that only by the VHF wavelength. VHF radar rms slopes of the mare surface range from about 1° to a little larger than 2°, indicating a smooth surface.

LAC 56 east (fig. 2). VHF rms slopes remain small across the mare surfaces ranging between about 1° and 4°. S-band rms slopes are in general larger than those of the VHF but locally they are about the same. They range between about 2° and 4°. There are no striking associations between features such as ridges and craters and the radar rms slopes.

LAC 57 west (fig. 3). The smooth mare surfaces across LAC 57 west have lower rms slopes for the VHF wavelength than those described above. Here the values range from a fraction of 1° to about 2°. At the S-band wavelength, rms slopes are generally between 2° and 4° and everywhere larger than the corresponding VHF values. At the eastern edge, S-band rms slopes increase abruptly to about 6°. This increase is associated with an increase in craters and visual roughness near 41° W. longitude.

LAC 57 east (fig. 4). Although VHF rms slopes remain low and show little relationship with the variable terrain here, S-band rms slopes are variable and apparently are associated with visible features. At the western edge, rms slopes are near 6°, but decrease to 4° across the smooth-appearing surfaces near 40° W. The rms slopes rise again over the rougher terrain near 39.5° W. and then decrease to about 4° across the smooth-appearing surfaces. Note the decrease in S-band values for the mare near 36.4° W. A rise of 5° to 6° occurs near the hills at 35° to 35.6° W. Eastward the surface is fairly smooth except for local roughness peaks that may correspond to small crater groups (such as those at 31.7° W.).

LAC 76 west and a small part of LAC 58 (fig. 5). Here a striking correlation

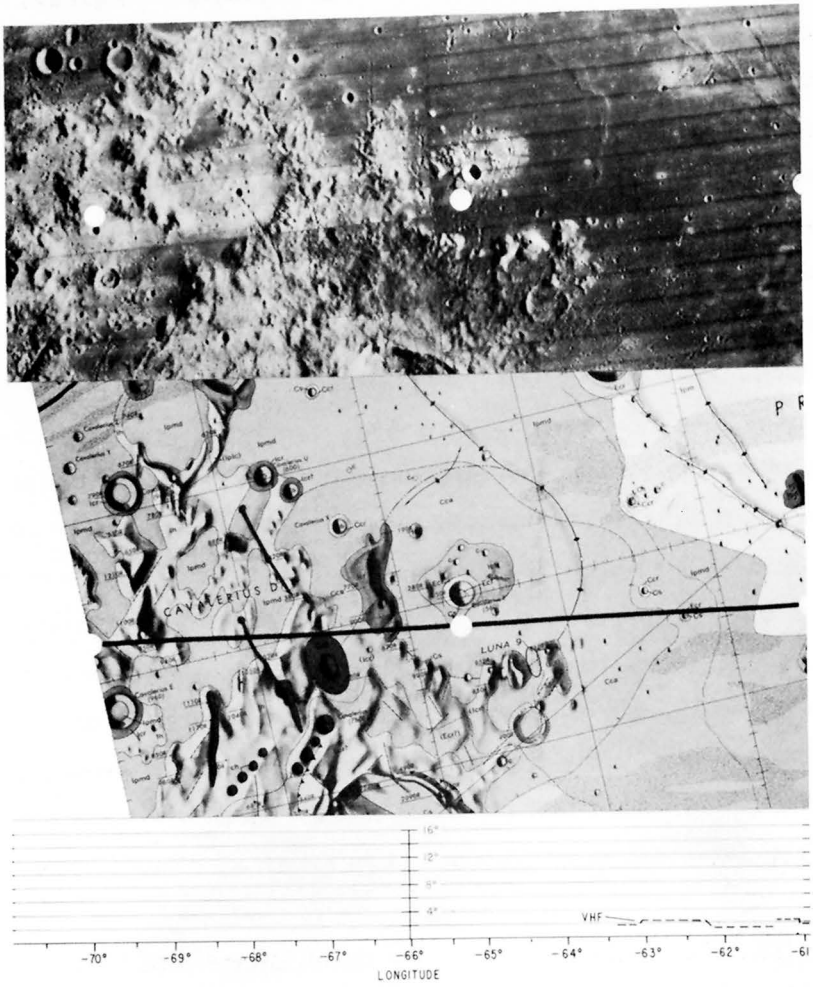

Bistatic Radar Estimates of RMS Slopes, Hevelius Quadrangle (LAC 56)

Figure 1. Image mosaic, geologic map, and bistatic-radar rms slopes in the western part of the Hevelius quadrangle (McCauley, 1967; LAC 56). White dots in mosaic indicate points along the Apollo 14 bistatic-radar specular track and indicate approximate size of area resolution cells. A similar representation is used for the geologic map. Line on graph indicates hand calculated VHF rms slopes as a function of longitude. Lunar Orbiter IV high resolution frames $169H_1$ and H_2 and $162H_1$ and H_2.

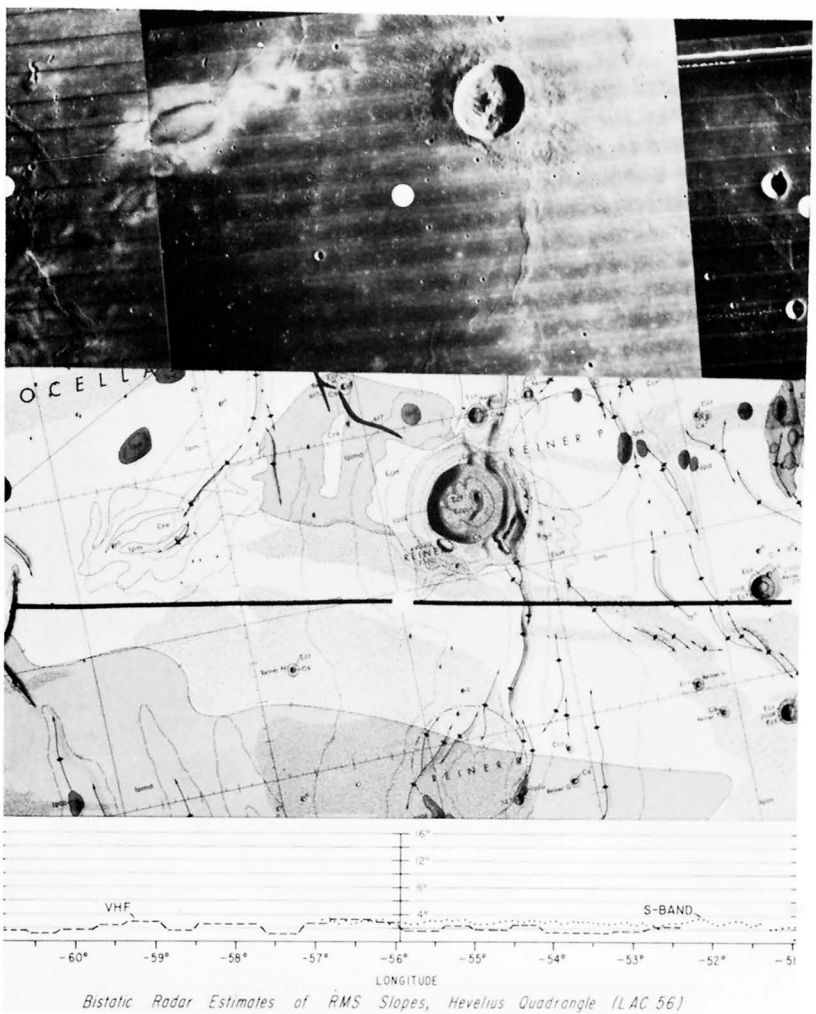

Figure 2. Image mosaic, geologic map, and bistatic-radar results in the central and eastern part of the Hevelius quadrangle (McCauley, 1967; LAC 56). White dots in mosaic indicate points on Apollo 14 bistatic-radar ground track and indicate approximate size of area resolution cells. White dots and line on geologic map indicate Apollo 14 bistatic-radar ground track. Lines on graph indicate hand calculated S-band and VHF rms slopes as a function of longitude. Lunar Orbiter IV high resolution frames $162H_1$, $157H_1$, and $150H_1$.

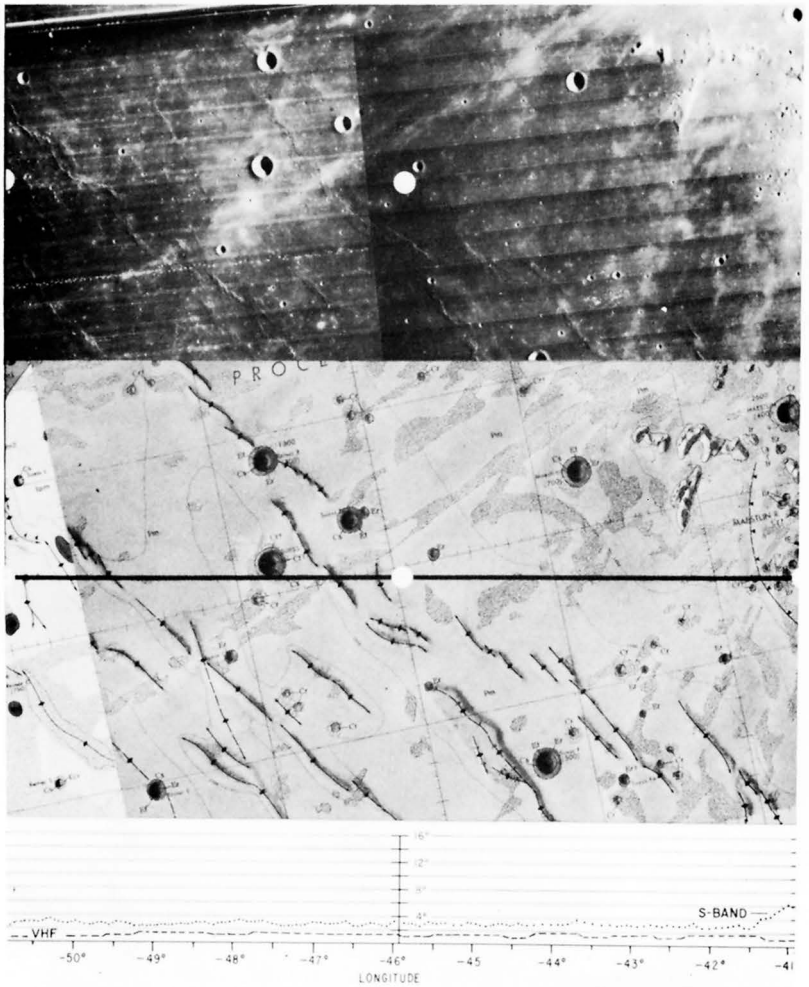

Bistatic Radar Estimates of RMS Slopes, Kepler Quadrangle (LAC 57)

Figure 3. Image mosaic geologic map, and bistatic-radar results in the western part of the Kepler region (Hackman, 1962; LAC 57). A small part of Hevelius quadrangle is included. Symbols and graph explained in figure 2. Note marked increase in S-band rms slopes near 41° west longitude and corresponding increase in roughness shown in mosaic. Lunar Orbiter IV high resolution frames 150 H_1 and 144 H_1.

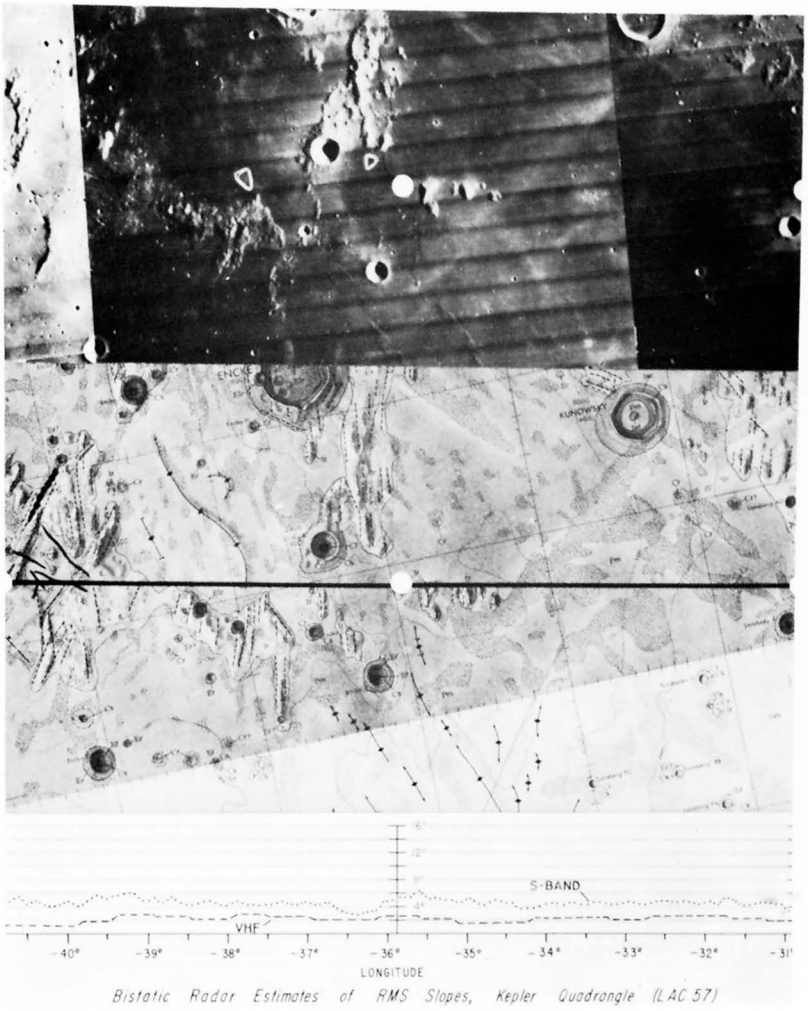

Figure 4. Image mosaic, geologic map and bistatic-radar results in the eastern part of the Kepler region (Hackman, 1962; LAC 57). A small part of the Letronne quadrangle is included. Symbols and graph explained in figure 2. Note S-band rms slopes are roughly twice the VHF rms slopes and low values of VHF rms slopes for the mare surfaces. Lunar Orbiter IV high resolution frames 144 H_1, 138 H_1, and 133 H_1.

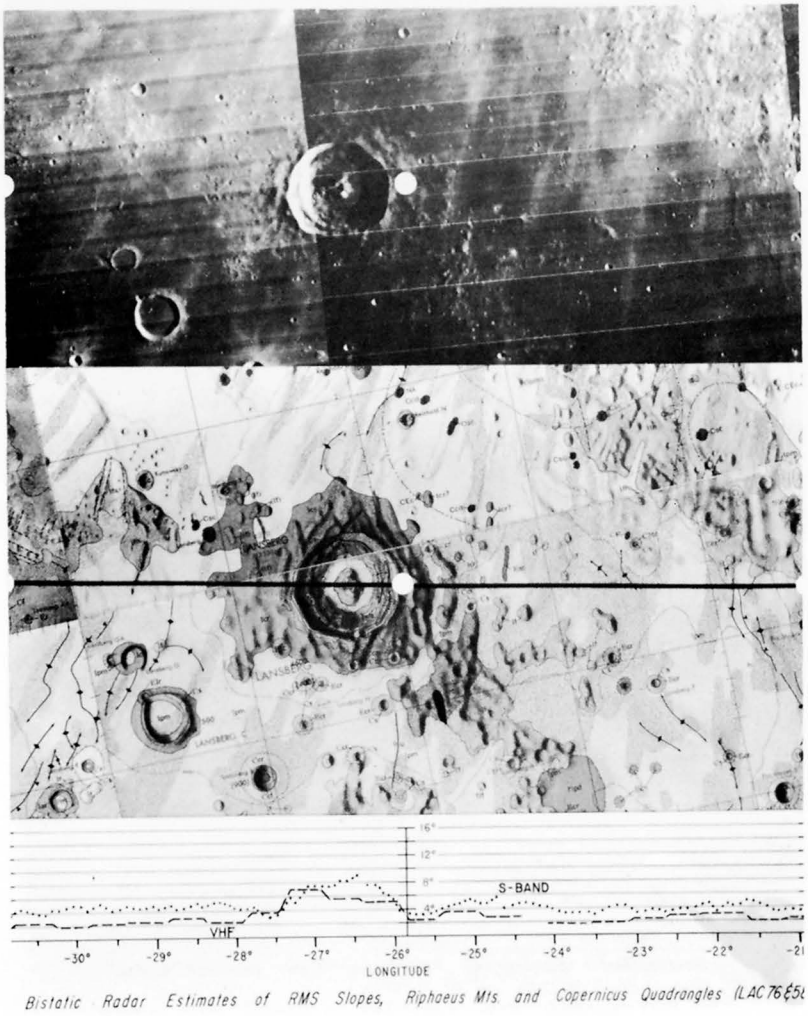

Figure 5. Image mosaic, geologic map, and bistatic-radar results in the western part of the Riphaeus Mountains region (Eggleton, 1965; LAC 76) and Copernicus quadrangle (Schmitt, Trask, and Shoemaker, 1967; LAC 58). Small parts of Letronne and Kepler quadrangles are included. Symbols and graph explained in figure 2. Note strong increase in S-band and VHF rms slopes across the crater Lansberg. Lunar Orbiter IV high resolution frames 133 H_1 and 126 H_1.

between the image and rms slopes occurs at the crater Lansberg (26.5° W.). At Lansberg, VHF rms slopes increase to values of 5° to 7° and S-band rms slopes climb to about 9°.

LAC 76 east (fig. 6). This region is different from previous ones both visually and in radar response. At the western edge VHF rms slopes rise to equal those obtained at S-band. Eastward this equivalence of S-band and VHF rms slopes is maintained. Visual roughness due to hummocky terrain is apparent between 16° and 18° W. Craters are abundant on the mare surface east of 16° W. The visually smooth surfaces in the west also appear smooth to the radar. For most of this track, rms slopes for both radars are near 4° to 6° for both the mare and hummocky terrain.

LAC 77 west (fig. 7). Here striking correlations between visual impressions of the image and the radar values of rms slopes are found. Where the radar ground track crosses Lalande (8.6° W.), Herschel DA (4° W.), and Herschel (2° W.), VHF rms slopes climb above the general local background to values of 7° to 8° and S-band rms slopes reach values between 8° to 11°. Between these craters, both VHF and S-band rms slopes are generally large (4° to 6°) and nearly the same. In contrast to previous areas, VHF rms slope values are occasionally larger than S-band values.

LAC 77 east (fig. 8). This entire area is rough and the topography is dominated by large ridges, depressions, craters, and relatively smooth but heavily cratered plains. Bistatic-radar results show the area is, indeed, rough. Most of the VHF rms slopes are between 5° and 7° and S-band rms slopes are chiefly between 6° and 8°. S-band rms slopes near the crater at 8° E. longitude appear anomalously small, while those in Gylden (0°) appear to correlate with the image.

LAC 78 west (fig. 9). The mosaic shows this section of the track is similar to LAC 77 east. VHF rms slopes are large and typically 5° to 8°. Near 17° E. they rise to almost 12°. S-band rms slopes are usually between 6° and 8° but locally smoother and rougher regions occur. VHF rms slopes are frequently larger than S-band rms slopes.

LAC 78 east (fig. 10). As in the previous section, the area is generally rough both visually and to the radar. Some areas appear smooth in the image and to the radar (28.5° E., for example), whereas others appear rough in the image

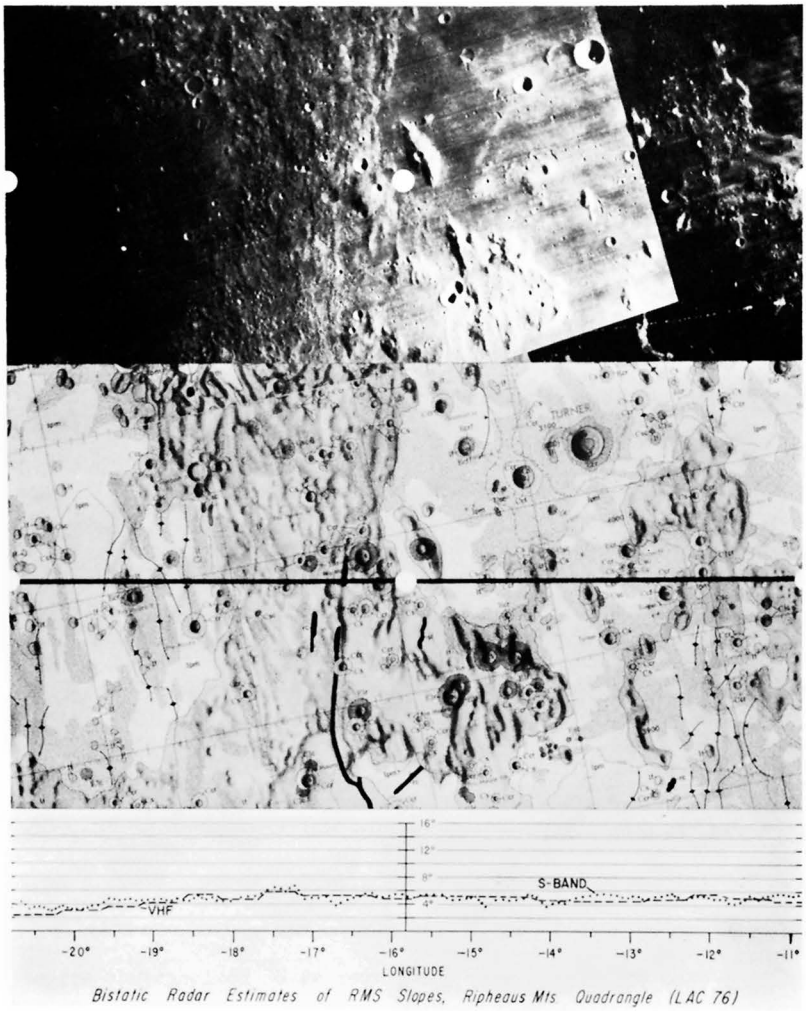

Figure 6. Image mosaic, geologic map, and bistatic-radar results in the eastern part of the Riphaeus Mountains region (Eggleton, 1965; LAC 76). Symbols and graph explained in figure 2. Note that both VHF and S-band rms slope values are equal and near 4° to 6° over much of the track. Lunar Orbiter IV high resolution frames 120 H_3 and 113 H_3.

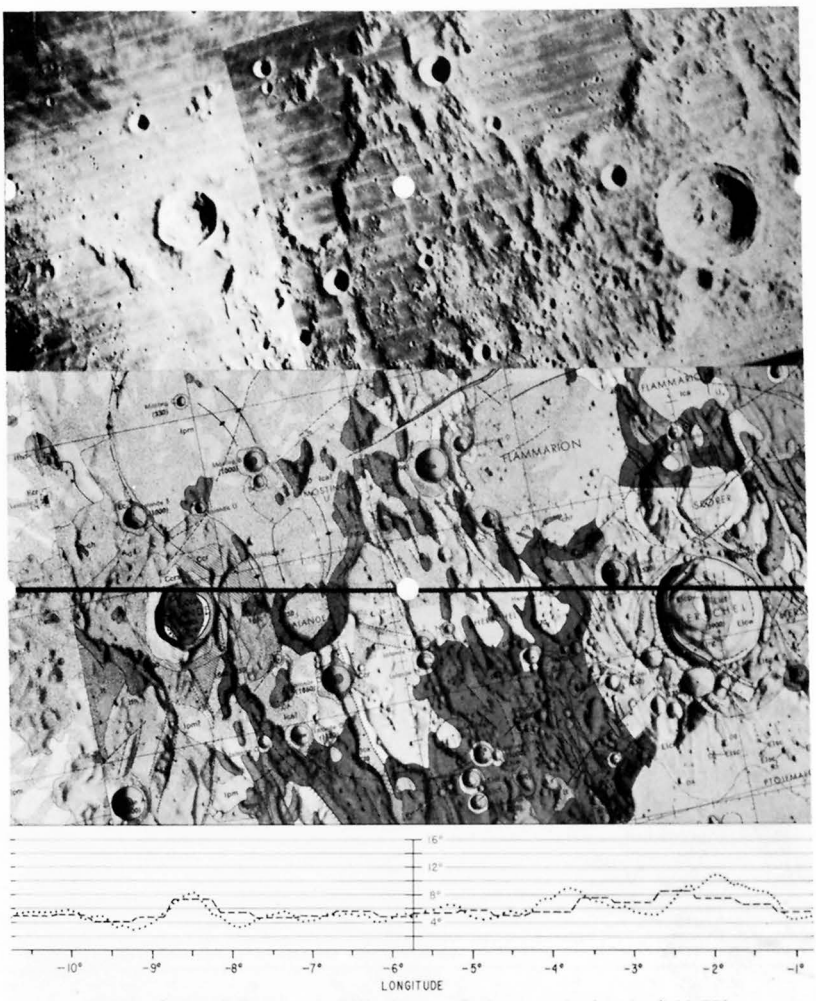

Figure 7. Image mosaic, geologic map, and bistatic-radar results in the western part of the Ptolemaeus quadrangle (Howard and Masursky, 1968; LAC 77). Symbols and graph explained in figure 2. Note correlation of radar rms slope values with craters Lalande (8.6° W), Herschel DA (4° W), and Herschel (2° W). Lunar Orbiter IV high resolution frames 113 H_3 and 108 H_3.

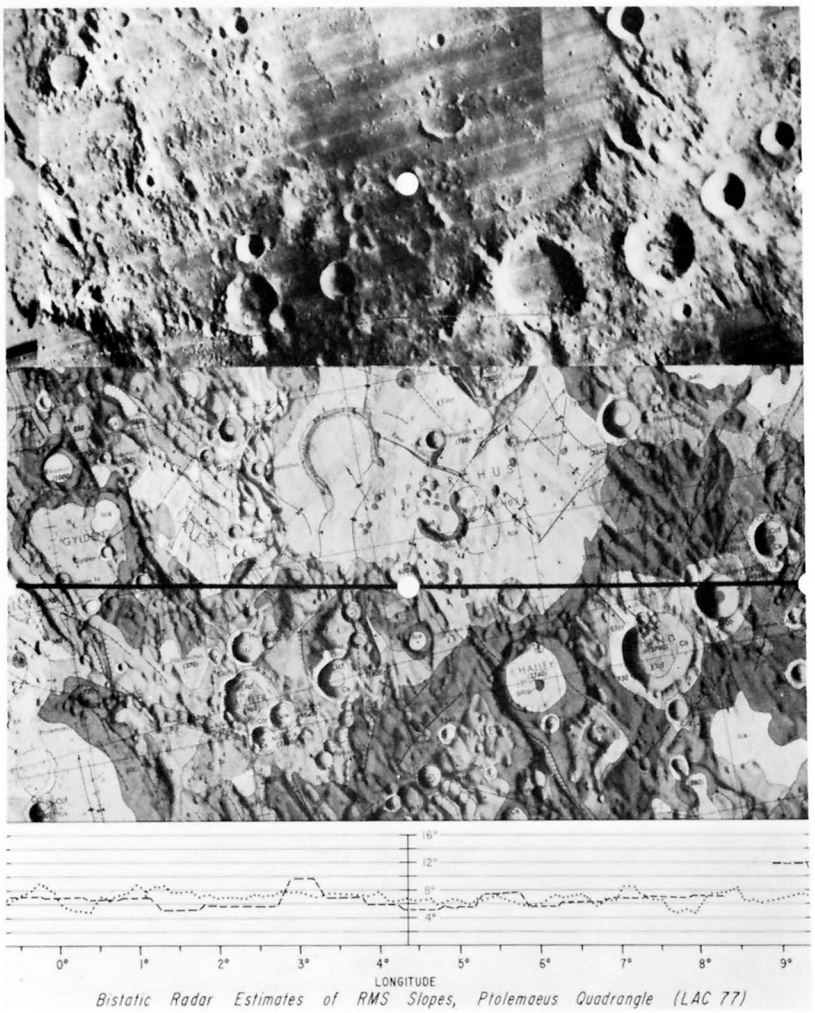

Figure 8. Image mosaic, geologic map, and bistatic-radar results in the eastern part of the Ptolemaeus quadrangle (Howard and Masursky, 1968; LAC 77). Symbols and graph explained in figure 2. Note very large rms slopes for both radars and rugged appearance of surface in images. Lunar Orbiter IV high resolution frames 103 H_3, 101 H_3, and 96 H_3.

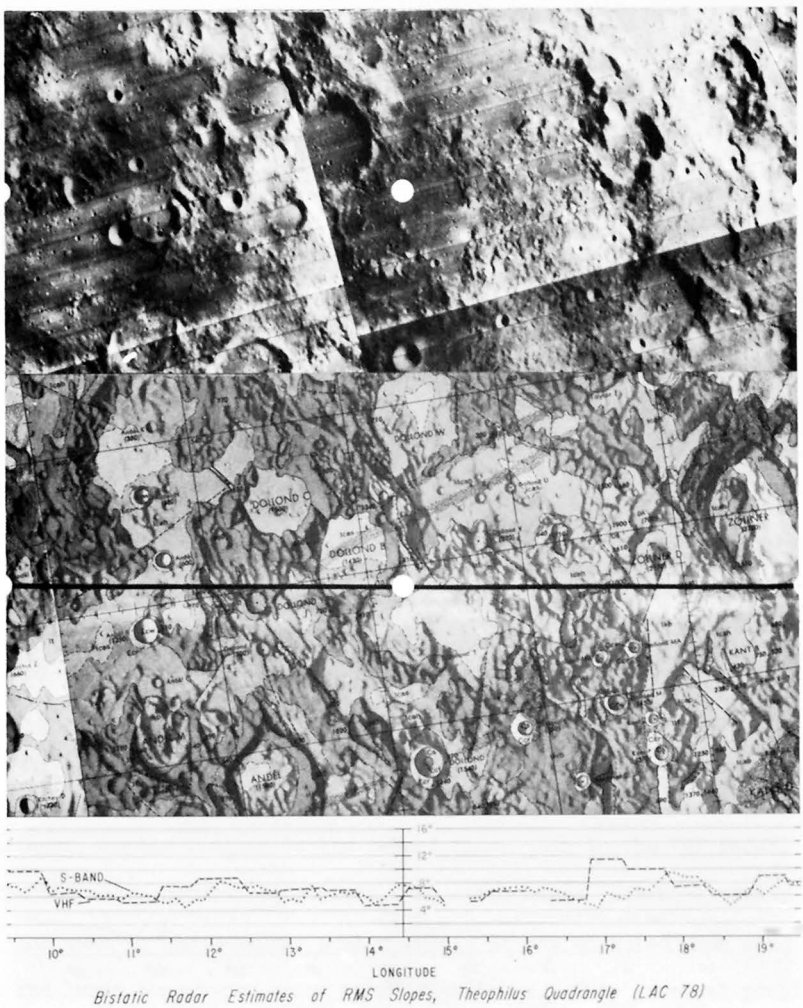

Figure 9. Image mosaic, geologic map, and bistatic-radar results in the western part of the Theophilus quadrangle (Milton, 1968; LAC 78). A small part of the Ptolemaeus quadrangle is included. Symbols and graph explained in figure 2. Note that VHF rms slopes locally exceed the S-band rms slopes and both are relatively large. Lunar Orbiter IV high resolution frames 96 H_2, H_3, and 89 H_2, H_3.

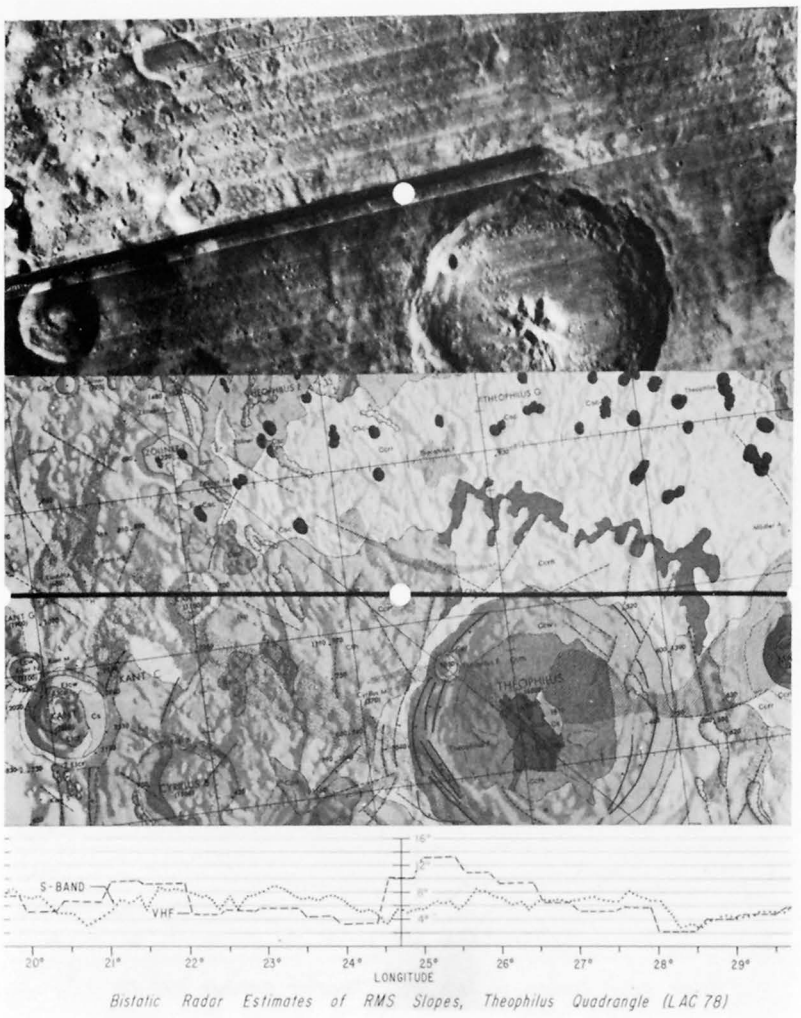

Figure 10. Image mosaic, geologic map, and bistatic-radar results in the eastern part of the Theophilus quadrangle (Milton, 1968; LAC 78). Symbols and graph explained in figure 2. Note smooth surface in image near 28.3° E. and corresponding low values of S-band and VHF rms slopes. Lunar Orbiter IV high resolution frames 89 H_2, H_3, and 77 H_2, H_3.

but smooth to the radar (at 20.7° E., for example). The west flank of Theophilus appears very rough to the VHF but not the S-band.

LAC 79 west (fig. 11). In this area, surfaces become visually smoother except near the crater Gaudibert (37° to 38.5° E.). Both VHF and S-band rms slopes are commensurate with this impression. Generally, rms slopes of both radars have decreased to between 4° and 6° except near some craters where they rise above 8°.

LAC 79 east (fig. 12). Both VHF and S-band rms slopes increase to about 6° south of Gutenberg, as they should, judging from the image. Eastward VHF rms slopes tend to decrease across uplands plains. Still further east across the smooth mare surfaces, VHF rms slopes decrease to about 1° to 2°. The low values of S-band rms slopes near 40° E. are anomalous in this region where the image appears rough.

LAC 80 west (fig. 13). Here VHF roughness remains low across smooth mare surfaces and rises somewhat as the flank of Langrenus is approached. VHF rms slopes are comparable to those in figure 1 (LAC 56).

It is clear from the foregoing discussion that visual impressions of roughness obtained from the images and bistatic-radar compare very well, although not perfectly. Visually smooth mare surfaces have the lowest VHF and S-band rms slopes. At least two types of mare surfaces can be recognized. Visually rough craters and uplands have the largest rms slopes. Many surfaces, particularly smooth mare surfaces, appear rougher to the S-band radar than to the VHF radar, as would be expected under natural conditions. In other cases, surfaces appear rougher to the VHF than to the S-band. Such a result is not expected from studies of terrestrial and lunar topography using other techniques. This reversal problem is discussed later. Theoretical implications of the bistatic-radar rms slopes and their wavelength dependence have been discussed elsewhere (Tyler and Howard, 1973).

B. Areal correlation of terrestrial remote sensing data

Although the previous section shows the correlation of the bistatic-radar with topography along a linear track, it is important that correlation of terrestrial radar with topography be illustrated using an area of the Moon (fig. 14), because the depolarized echo strengths show a clear correlation with topography. In particular, Earth-facing slopes typically produce large echoes. A similar

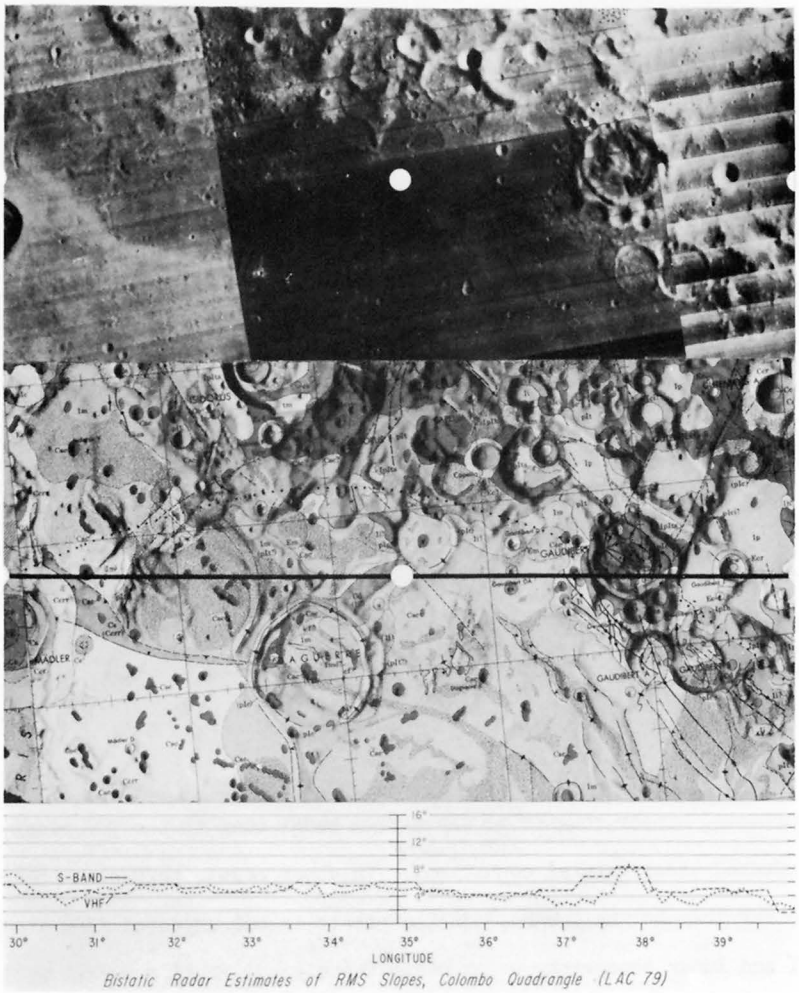

Figure 11. Image mosaic, geologic map, and bistatic-radar results in the western part of the Colombo quadrangle (Elston, 1972; LAC 79). A small part of the Theophilus quadrangle is included. Symbols and graph explained in figure 2. Lunar Orbiter IV high resolution frames 77 H_2, H_3, 72 H_2, H_3, and 65 H_2, H_3.

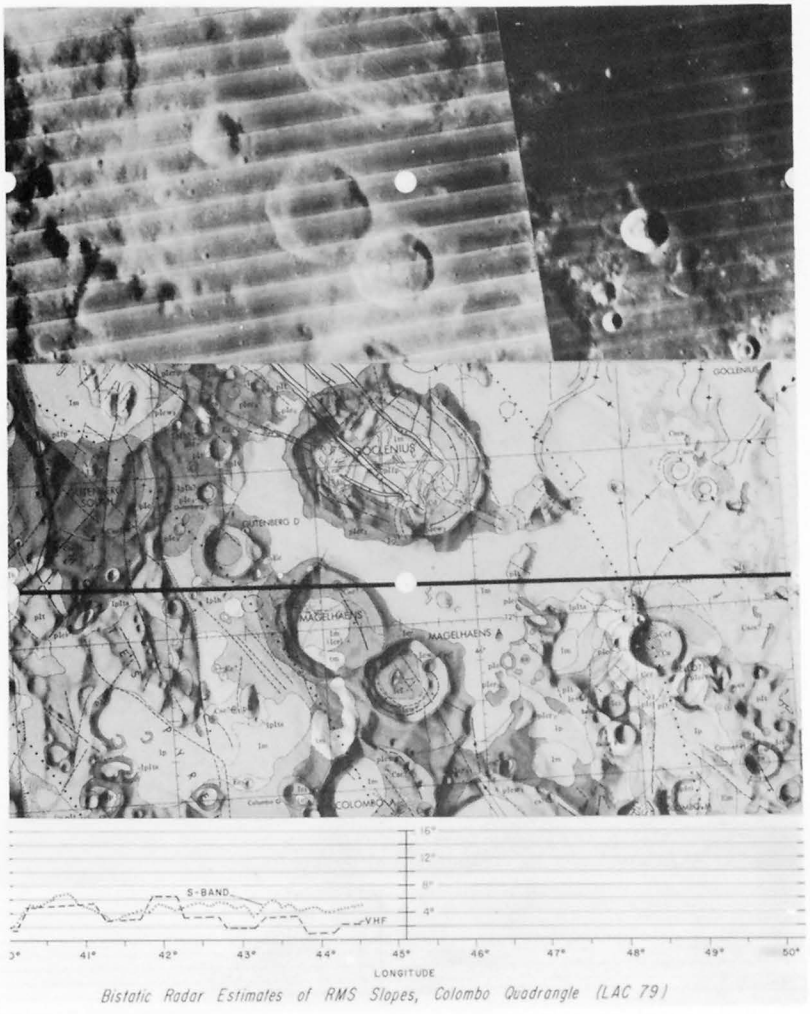

Bistatic Radar Estimates of RMS Slopes, Colombo Quadrangle (LAC 79)

Figure 12. Image mosaic, geologic map, and bistatic-radar results in the eastern part of the Colombo quadrangle (Elston, 1972; LAC 79). A small part of the Langrenus quadrangle is included. Symbols and graph explained in figure 2. Plot of rms slopes stops because most of subsequent analyses exclude data between 44.5° and 51.0° E. Lunar Orbiter IV high resolution frames 65 H_2 and 60 H_2.

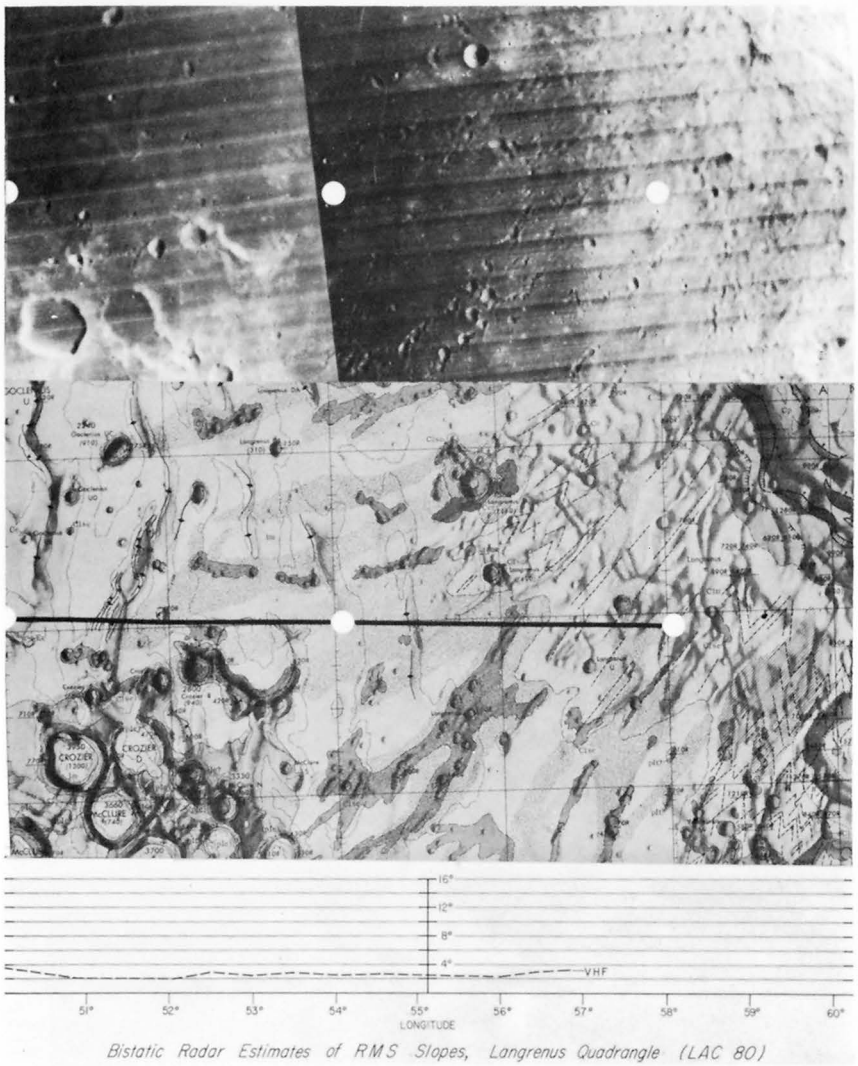

Figure 13. Image mosaic geologic map, and bistatic-radar results in the western part of the Langrenus quadrangle (Hodges, 1973; LAC 80). Symbols and graph explained in figure 1. Note low VHF rms slopes across smooth mare surfaces. Lunar Orbiter IV high resolution frames 60 H_2 and 53 H_2.

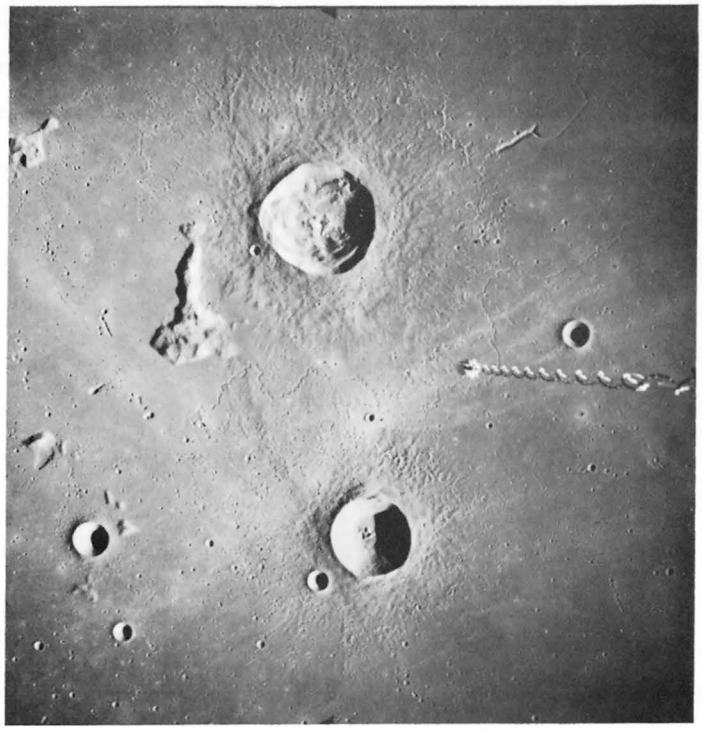

Figure 14. Delisle-Diophantus area in the northwest quadrant of the Moon (coordinates of center of figure are 28°50' N. and 34°30' W.). Large crater, upper center, is Delisle (≈ 27 km across); large crater, lower center, is Diophantus (≈ 19 km across). Rod at right center is part of spacecraft. Apollo 15 metric camera photograph (AS-15-2188).

slope dependence is not evident in the infrared eclipse temperature.

The Delisle-Diophantus area in the northwest quadrant of the Moon ($28^{\circ}50'$N.; $34^{\circ}30'$W.) was selected to illustrate the correlation of echo strength with slope. This correlation is clearly evident on contour maps of both 3.8 cm and 70 cm depolarized radar echoes. Strong echoes correlate with steep Earth-facing slopes (figs. 14, 15, and 16; see also, Moore and Zisk, 1974). Within Delisle ($\approx$ 27 km across) and Diophantus ($\approx$ 19 km across), the largest echoes within the entire area coincide with the Earth-facing slopes of the northwest crater walls. The 3.8 cm echoes--the two km resolution is used here--from the northwest wall of Diophantus exceed 4.[1/] Those from the southwest and northeast walls are near 3.4 to 3.7 and those from the southeast walls are near 3.1 to 3.4. This effect of slope is seen in Delisle and the smaller craters Diophantus A, B, C, and D (A, B, C, and D in fig. 15). Delisle illustrates the effect of slope on its flanks where echoes from the Earth-facing slopes of the southeast flank are 3.1 to 3.4; those on the northeast and southwest flanks are 2.8 to 3.1; and values of 2.5 to 2.8 occur on the northwest flank. Echoes from Delisle are generally lower than those from Diophantus. The mountain southwest of Delisle has values substantially smaller than those of Delisle although there are steep Earth-facing slopes. Echoes from this mountain with values of 2.8 to 3.1 tend to occur on Earth-facing slopes while lower values of 2.5 to 2.8 occur on slopes facing the opposite direction.

Although the distribution of echoes with respect to slope orientation shows the effect of topography, the relative values of large echoes from Earth-facing slopes in Diophantus, Delisle, and the mountain southwest of Delisle show that a second factor is involved. This is probably due to the relative abundance of rock fragments and blocks at and near the surface. Inspection of Apollo 15 panoramic camera photographs shows that blocks and rocks occur on the walls and flanks of Delisle and Diophantus but not on the nearby mountain. The two small craters between Delisle and Diophantus (no. 4 in fig. 15) are characterized by both relatively large echoes and a profusion of blocks in their ejecta. This is consistent with the interpretation that rock fragments and blocks contribute to the depolar-

---

1/ Echo strengths used here are in units of $\log_{10}$ of relative power (watts/watts-m^2):4 = 10^4 m^{-2}.

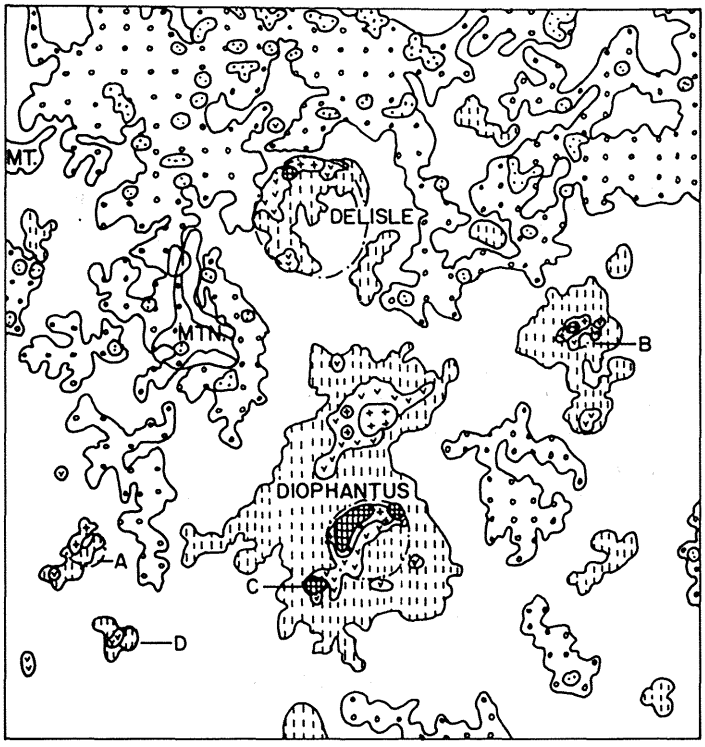

CONTOUR MAP OF 3.8 CM. DEPOLARIZED RADAR ECHOES
NEAR THE CRATERS DELISLE AND DIOPHANTUS

ECHO STRENGTH CONTOURS

> 4.0	2.8 - 3.1
3.7 - 4.0	2.5 - 2.8
3.4 - 3.7	< 2.5
3.1 - 3.4	Crater rim

Figure 15. Contour map of 3.8 cm depolarized radar echoes from the Delisle-Diophantus area of the Moon. Note largest echoes occur on Earth-facing slopes of northwest walls of craters.

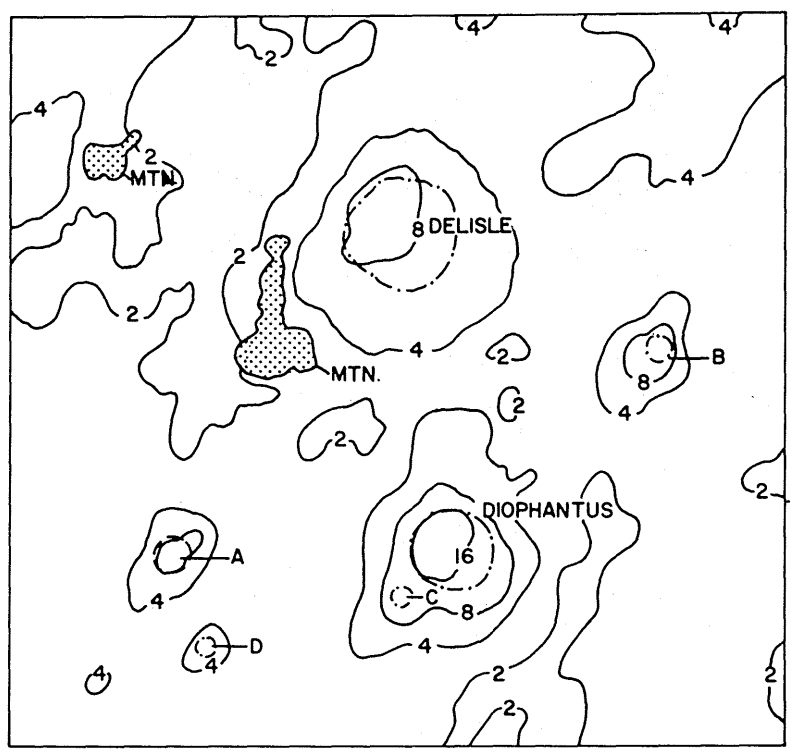

CONTOUR MAP OF 70 CM. DEPOLARIZED RADAR ECHOS
NEAR THE CRATERS DELISLE AND DIOPHANTUS
(CONTOUR INTERVAL IS LOG TO THE BASE 2)

Figure 16. Contour map of 70 cm depolarized radar echoes from the Delisle-Diophantus area of the Moon. Echo levels are log to the base 2. Thus, echo power at contour level 8 is twice that at level 6 and 4 times that at level 4, etc. Note largest echoes associated with Earth-facing slopes of northwest crater walls and small craters.

ized echoes (Thompson and others, 1974).

Frequency distributions of 3.8 cm depolarized radar echoes of the Delisle-Diophantus area (Moore and Zisk, 1974, fig. 33-3(c)) are approximately Gaussian for about 90 percent of the echo values. At echoes above 3.4, the curve deviates positively from the Gaussian curve and below 2.5 it deviates negatively. Values above 3.4 are associated with the interiors of craters, blocky craters, and bright-halo craters (craters 1, 2, 3, 4, and craters A, B, C, and D in fig. 15). Values below 2.5 are associated with relatively smooth mare surfaces.

The frequency distribution curves may indicate a generally random population of 3.8 cm radar echo strengths over the lunar surface slightly modified by a population of large echo strengths associated with fresh craters and their blocky ejecta. A third population yielding low echo strengths may be present. This population could arise from a locally thick regolith, a fine-grained, porous surficial unit, local smooth surfaces, or an electromagnetically absorbing material at the surface.

Contours of 70 cm depolarized echoes (fig. 16) also show that large echo strengths are associated with Earth-facing slopes within the craters but the effect is less pronounced due to the larger resolution cells. The 16 contour within Diophantus and the 8 contour within Delisle are found on the northwest parts of the craters. The centroid of the number 4 contour around Delisle is displaced toward the southeast flank from the crater center (fig. 16). Small craters Diophantus A, B, and D have large echoes and the number 4 contour encircling Diophantus is constrained to include the two bright ray craters with blocky ejecta just north of it. The number 8 contour includes Diophantus C. Thus high values are associated with craters and slopes. The mountain southwest of Delisle does not have large echoes associated with it despite steep Earth-facing slopes. Low echoes also appear to be associated with mare surfaces.

High infrared eclipse temperatures correlate with the same craters as do the strong radar echoes (fig. 17). Within the craters Delisle and Diophantus there is no evidence for a correlation between Earth-facing slopes and large eclipse temperatures.

C. Bistatic-radar roughness and geologic map units

The recognition and delineation of photogeologic map units are partly based

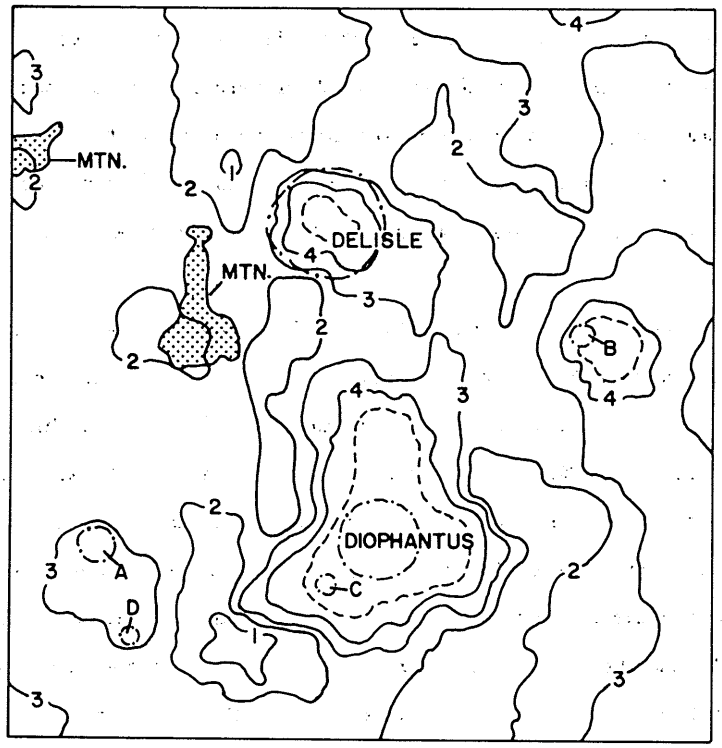

CONTOUR MAP OF INFRARED ECLIPSE TEMPERATURES
NEAR THE CRATERS DELISLE AND DIOPHANTUS

Figure 17. Contour map of infrared eclipse temperatures for the Delisle and Diophantus area of the Moon. The contour interval is 2 degrees Kelvin. Note contours enclosing high temperatures are centered near craters.

on their topographic expression. Thus a correlation between map units and bistatic-radar rms slopes should be expected. This is the case.

For this preliminary correlation effort, the surfaces have been grouped into eight broad units: 1) mare materials (Im), 2) dark mare materials (Imd), 3) all Copernican units (chiefly young craters: Ccr, Ccw, etc., and bright slopes, Cs; also the Cavalerius Formation, Cca), 4) Eratosthenian craters (Ec, Ecr, etc.), 5) Eratosthenian or Imbrian craters (EIcr, etc.), 6) Cayley Formation (Ica, Icas, Icah), 7) all Imbrian units except Cayley Formation and mare material, and 8) all pre-Imbrian units (pI). Mare materials (Im) are subdivided by the LAC chart in which they occur, and the Cavalerius Formation is considered separately (unit Cca). These subdivisions, which are shown in table 2, allow the results to be compared with those of previous terrain studies (Rowan and others, 1971). The radar results permit delineation of smooth mare, rough mare, various rougher terra terrains, and crater terrains, but at smaller slope lengths or larger scales than those of Rowan, McCauley, and Holme (1971).

Generally the averaged bistatic-radar rms slopes agree with expectations based on geologic map units (table 2). Departures can be explained as a function of sampling. Very rough parts of Eratosthenian or Imbrium craters (EI), when sampled, appear rough to the radar. The radar ground track sampled much of the walls and floor of Herschel (EIcr, etc. fig. 7). In contrast, samples from equally rough Copernican craters were chiefly from the flanks (Ccr), which are relatively smooth compared to the walls and floors of both the Copernican craters and the crater Herschel.

The correlation may be illustrated by comparing averaged or mean rms slopes of the S-band radar with those of VHF radar for the various geologic map units. As shown by figure 18a and b, the geologic map units fall into two broad categories using both hand and machine calculated rms slopes: (1) mare units which are smoother than other units (except the mare materials of LAC 77 and LAC 79), and (2) rough units of craters (C, E, EI), upland units in general (I, pI), and Cayley Formation (Ica). The plots for machine and hand calculated mean values are different. Machine calculated mean rms slopes cluster closer to the average (Apollo 14 Moon in fig. 18a) while those of the hand calculated averages are spread out more or less linearly (fig. 18b). Both plots, however,yield similar results. Mare

Table 2. Average values and standard deviations of machine and hand calculated rms slopes from S-band and VHF bistatic-radar along Apollo 14 bistatic-radar ground track for various geologic map units

	S-BAND BISTATIC-RADAR						VHF BISTATIC-RADAR					
	MACHINE CALCULATED			HAND CALCULATED			MACHINE CALCULATED			HAND CALCULATED		
	MEAN	σ	N	MEAN	σ	N	MEAN	σ	N	MEAN	σ	N
All geologic map units	5.02	1.28	1055	5.05	1.63	917	5.58	1.38	787	4.32	2.42	959
Mare materials (unit Im)	4.27	0.94	424	3.87	0.91	381	4.61	1.26	256	2.58	1.31	413
Dark mare materials (unit Imd)	3.27	0.27	20							1.68	0.49	11
Copernican craters and slopes (units C--)	5.17[1] (5.84)	1.43	170[1] (126)	5.83	1.40	124	6.29	1.04	123	5.96[2] (6.18)	2.55	128[2] (121)
Eratosthenian craters (unit E--)	6.16	1.40	45	6.52	2.21	44	6.00	0.87	41	6.16	1.40	43
Eratosthenian-Imbrium craters (unit EI--)	6.84	0.62	34	7.29	1.82	34	5.80	0.75	34	6.70	0.81	34
Cayley Fm (units Ica, Icas, Icah)	6.13	0.44	34	6.08	0.71	35	5.96	0.82	35	6.22	1.40	35
All I units (except Cayley, mare)	5.53	1.04	237	5.64	1.54	209	5.74	1.22	209	5.32	2.15	209
All pre-Imbrian (units pI--)	6.07	0.73	116	6.19	1.30	116	6.42	1.28	115	5.99	2.10	112
Mare 79 (unit Im on LAC 79)	5.13	0.42	40	4.78	0.55	40	6.79	0.96	40	5.07	0.62	40
Mare 77 (unit Im on LAC 77)	5.56	0.25	5	5.09	0.57	5	4.62	0.57	5	4.66	0.53	5
Mare 76 (unit Im on LAC 76)	5.04	0.42	86	4.30	0.63	90	4.26	0.84	88	3.48	1.20	88
Mare 58 (unit Im on LAC 58)	5.08	0.29	16	4.52	0.35	16	3.97	0.56	16	2.35	0.34	16
Mare 57 (unit Im on LAC 57)	4.28	0.77	164	3.68	0.89	165	4.19	0.86	107	1.80	0.51	165
Mare 56 (unit Im on LAC 56)	3.20	0.44	113	2.93	0.36	65				2.02	0.71	99
Cca (unit Cca on LAC 56)	3.25		44							2.11	--	7

1/ Forty-four points of mare-like Cca included. Number in parentheses is adjusted for young craters and slopes with unit Cca removed. Mean for unit Cca listed with mare units.

2/ Seven points of mare-like Cca included. Number in parentheses is adjusted for young craters and slopes with unit Cca removed. Mean for unit Cca listed with mare units.

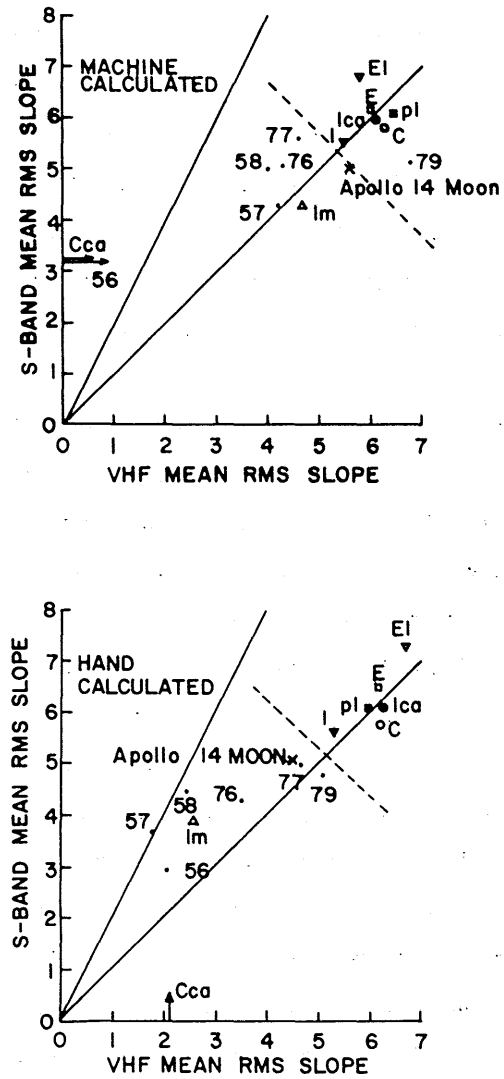

Figure 18. Averaged or mean S-band and VHF rms slopes for various geologic map units: (a) machine calculated values and (b) hand calculated values. Designators are: (1) Apollo 14--all geologic units, (2) C--Copernican crater units and bright slope material, (3) E--Eratosthenian crater units, (4) EI--Eratosthenian-Imbrian crater units, (5) I--all Imbrian units except mare materials and Cayley Formation, (6) pI--all pre-Imbrian units, (7) Ica--Cayley Formation, (8) Im--all mare material averaged, (9) Cca--Cavalerius Formation, and (10) 56, 57, 58, 76, 77, and 79--mare materials in LAC charts 56, 57, 58, 76, 77, and 79. Solid lines represent loci of points where S-band rms slopes are twice those of the VHF rms slopes and where they are equal. Dashed lines show separation between mare and upland-crater units.

materials in LACs 56, 57, 58 and 76, and unit Cca are relatively smooth compared to the mare materials in LAC 77 and 79. Of the rough units, I is the smoothest and EI (craters) is the roughest to the S-band. In a manner similar to Rowan, McCauley, and Holme (1971), maria may be divided into smooth (Im in LACs 56 and 57), rough (Im in LACs 58 and 76), and very rough (Im in LACs 77 and 79). Subdivision of upland and crater units is difficult. The roughness of the only upland plains unit separated (Cayley Formation, Ica) is noteworthy since it appears rougher than all mare units (except to machine calculated VHF averaged values of Im in LAC 79).

Frequency distributions of rms slopes for various units illustrate the local variations typical of most terrain, enforce the results discussed above, and indicate further subdivisions in keeping with previous interpretations discussed above. Cumulative frequency distributions of machine calculated S-band rms slopes are plotted in figures 19a and b on probability paper; some are approximately linear (units pI and Im of LACs 56 and 76) whereas others have flexures (all geologic units, and all mare material, unit Im). The flexure in the curve for all geologic units can be accounted for by a mixture of smooth mare units and rougher upland and crater units. In a similar fashion, mare materials (unit Im) and mare material in LAC 57 are composed of two mare types: (1) mare materials in LAC 76 and (2) mare materials in LAC 56. Frequency distributions of hand calculated S-band rms slopes yield similar results although they tend to be more linear (figs. 20a, b). Again the flexure in the curves for the maria (unit Im) suggest a mixture of two types, especially in LAC 57. Inspection of figures 3 and 4 will show the flexure is related to a mixture between the smooth mare west of long 42.5° W. and rough mare east of long 42.5° W.

Cumulative frequency distributions of machine calculated VHF rms slope tend to be linear except for mare material (figs. 21a, b). The individual mare units plotted (Im in LAC 56 and 76) are nearly linear for the middle 80 percent of the sample. Distributions of hand calculated VHF rms slopes for the various units are typically non-linear although individual mare units are nearly linear (figs. 22a, b; Im in LAC 56 and 57).

D. Terrestrial radar and geologic map units

Comparison of depolarized echoes for the 3.8 cm terrestrial radar with those

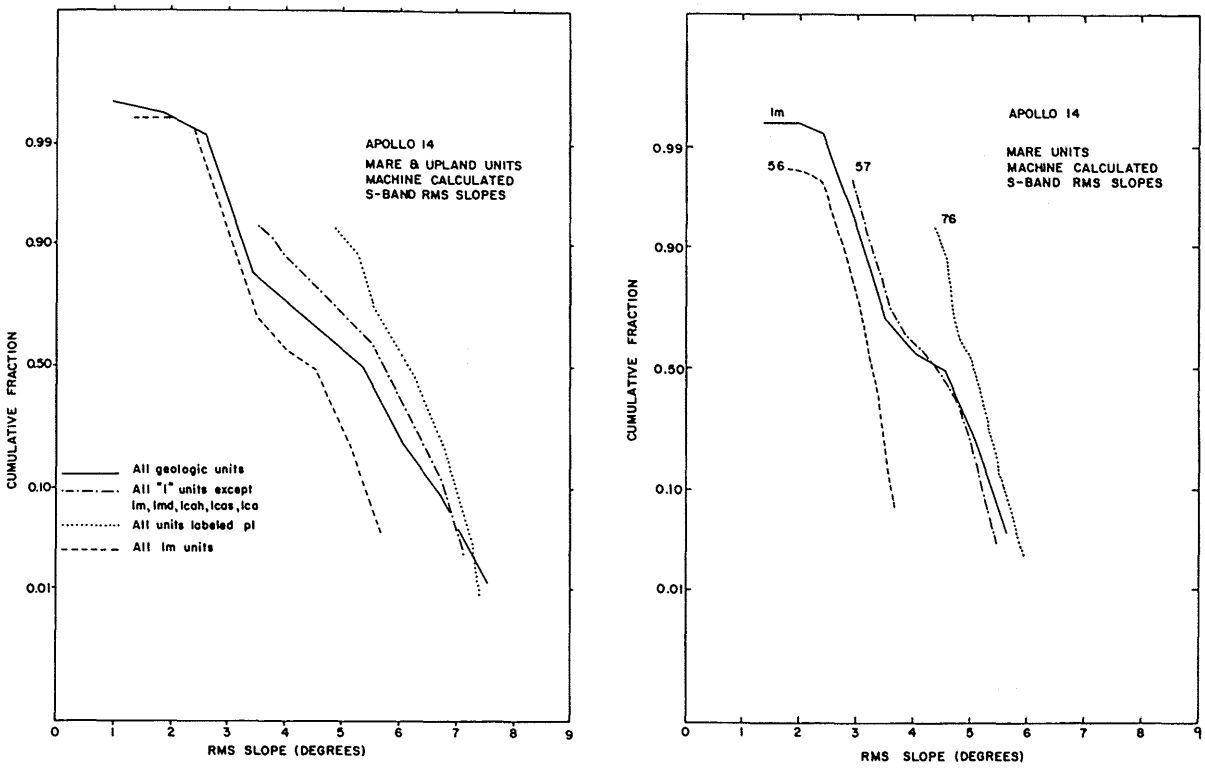

Figure 19. Frequency distributions of machine calculated S-band bistatic-radar rms slopes plotted on probability paper: (a) for all geologic units, all mare units (all Im), all Imbrian units (except Im, Imd, Icas, Icah, and Ica), and all pre-Imbrian units (all pI); and (b) for all mare materials (Im), mare material in LAC 56 (56), mare material in LAC 57 (57), and mare material LAC 76 (76). Note flexures in distributions for all geologic units and mare material (Im) and nearly linear form of all pre-Imbrian units (pI) in figure a. Flexure also characterizes distribution of rms slopes for mare material in LAC 57 but those of LAC 56 and 76 in b are nearly linear.

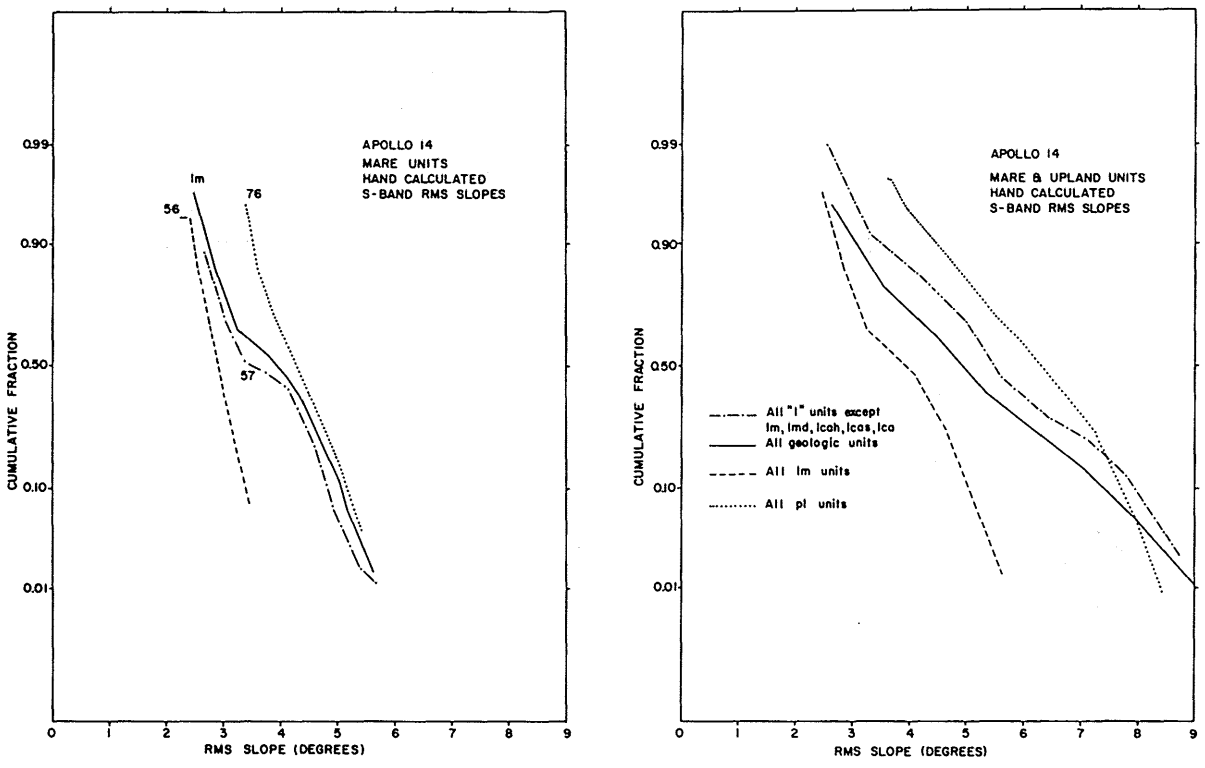

Figure 20. Frequency distributions of hand calculated bistatic-radar rms slopes plotted on probability paper: (a) for all geologic units, all mare units (all Im), all Imbrian units (except Im, Imd, Icah), and all pre-Imbrian units (all pI); and (b) for all mare materials (Im), mare material in LAC 56 (56), mare material in LAC 57 (57), and mare material in LAC 76 (76). Note flexure in distribution for mare material and approximate linearity of distribution of pre-Imbrian units (pI). Flexure also characterizes distribution for mare material in LAC 57 (57) while those in LAC 56 and 76 are nearly linear in b.

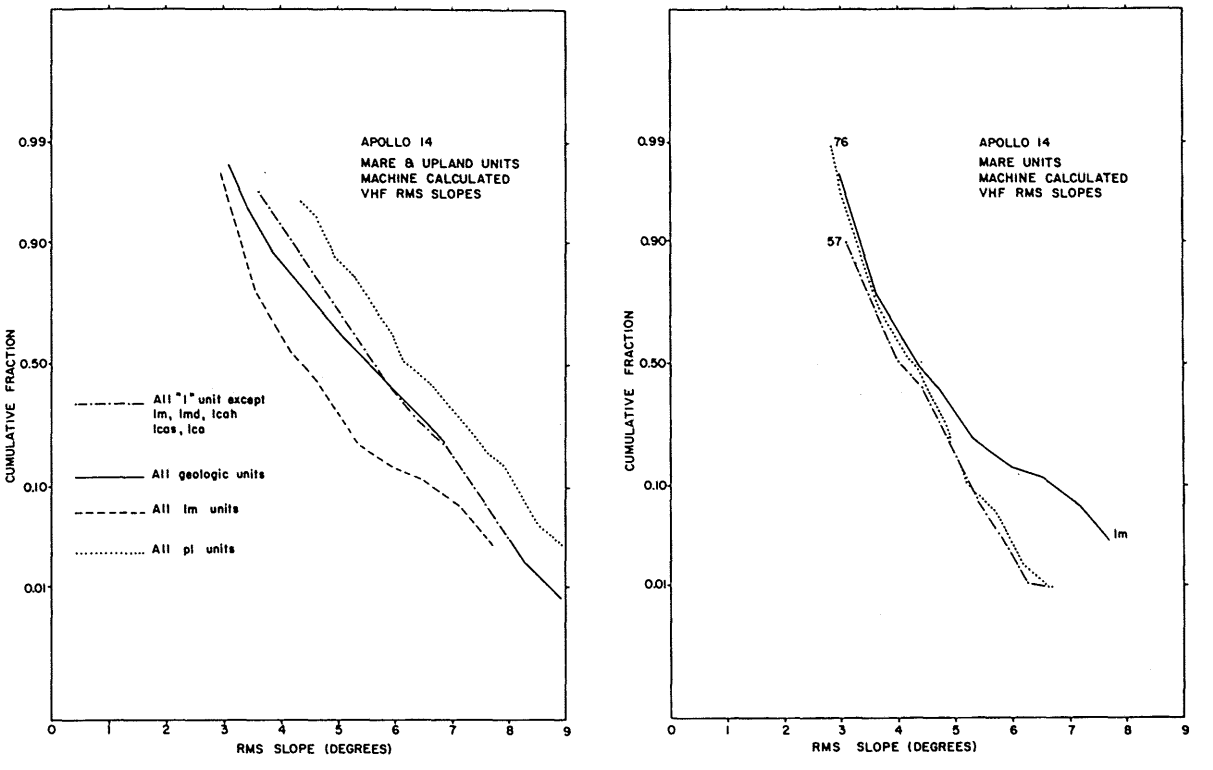

Figure 21. Frequency distributions of machine calculated VHF bistatic-radar rms slopes plotted on probability paper: (a) for all geologic units, all mare units (all Im), all Imbrian units (except Im, Imd, Icas, Icah, and (Ica), and all pre-Imbrian units (all pI); and (b) for all mare materials (Im), mare material in LAC 57 (57), and mare materials in LAC 76 (76). Note flexure in distributions for mare material and linearity of distributions for all "I" and pI units in a. Mare material distribution in LAC 57 (57) is almost linear in b.

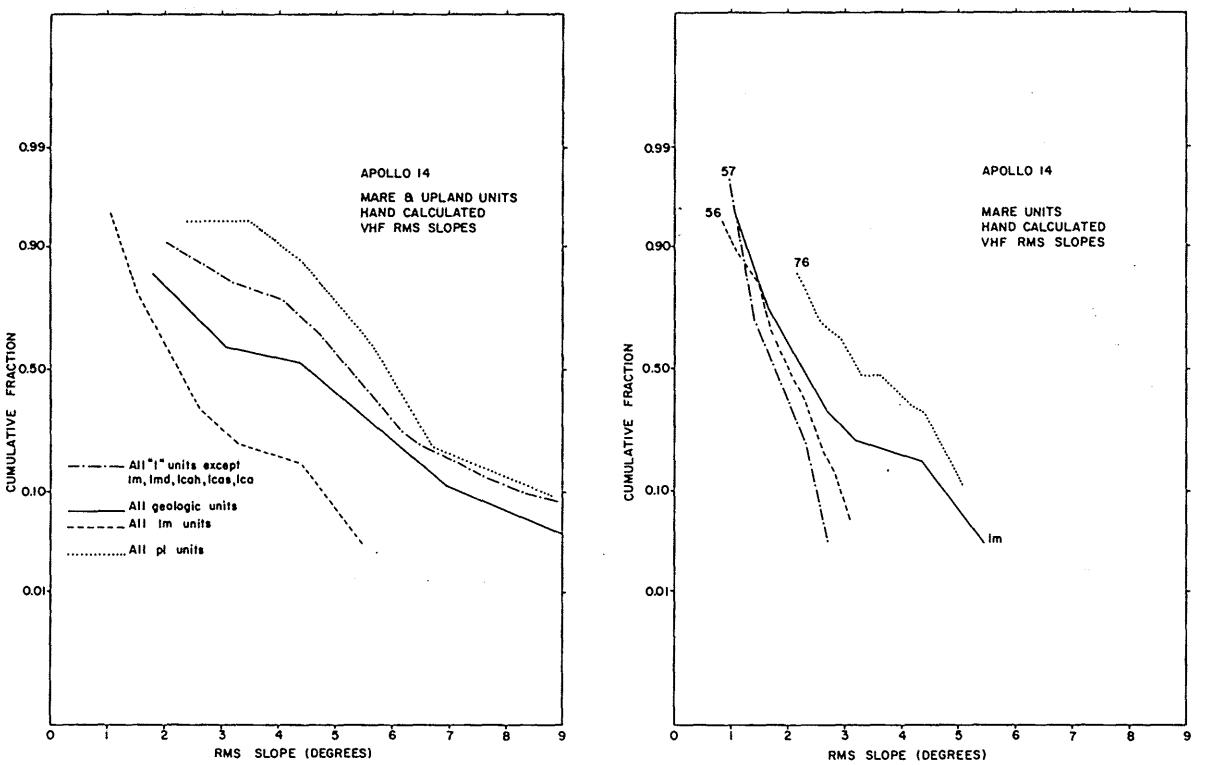

Figure 22. Frequency distributions of hand calculated VHF bistatic-radar rms slopes plotted on probability paper: (a) for all geologic units, all mare units (all Im), all Imbrian units (except Im, Imd, Ica, Icas, Icah), and all pre-Imbrian units (all pI); and (b) for all mare materials (Im), mare material in LAC 56 (56), mare material in LAC 57 (57), and LAC 76 (76). Note most curves are non-linear except mare materials in individual LAC charts.

of 70 cm radar for the various geologic map units yield similar results to those for the bistatic-radar (see table 3). This similarity is shown in figure 23 where averaged depolarized echoes of various geologic map units at 3.8 cm wavelength are plotted against those at 70 cm wavelength. As in the plots of S-band and VHF rms slopes (see fig. 18), geologic map units are separated into two categories: (1) mare materials (Im, Cca, and digits), and (2) crater and upland units (I, Ica, pI, C, E, and EI). Additionally, there is a strong positive correlation between the averaged echo strengths, suggesting a similarity in the cause of their responses. Lack of detailed parallelism exists particularly for mare materials. In contrast with the bistatic-radar results, mare material in LACs 76 and 79 are clearly separated from the crater and upland units and the mare materials in the various LAC areas, considered as a subset, are inversely correlated.

Frequency distributions of depolarized radar echoes reveal additional characteristics of the geologic map units: (1) echo values vary widely so that a given unit locally has values that are the same as those of other map units elsewhere, (2) some of the distributions are approximately Gaussian--especially the 3.8 cm echo distributions, and (3) many distributions have "tails" or positive departures from a generally linear trend at large echo values. The Gaussian character of the frequency distributions is shown in figure 24. "Tails" characterize the distributions for most geologic units; however, mare materials in LACs 56 and 76 do not have tails. The positive departure at large echo strengths in mare material can be ascribed to a specific group of features. In particular, the very large 3.8 cm echo strengths are due chiefly to the crater Suess and a bright crater just south of it (fig. 3, at 47.7° W.) where average echo values are 3.62--much larger than average mare surfaces which are 3.24 (see table 2). Positive departures or tails for upland and crater units are probably due to large Earth-facing slopes (see Moore and Zisk, 1973).

The tendency for normal distributions of the 70 cm radar depolarized echoes is not as marked as those of the 3.8 cm radar echoes, although mare material in general is markedly linear when plotted on probability paper (fig. 25). The tail or positive departure for mare material in LAC 57 can again be ascribed to the crater Suess and its bright companion crater to the southwest (fig. 3, at 47.7° W.) where average echoes are 136--much larger than the average mare which is 97 (see

Table 3. Average values and standard deviations of polarized and depolarized terrestrial radar echo and infrared eclipse temperatures for various geologic map units along the Apollo 14 bistatic-radar track.

	3.8 cm Radar Echos						70 cm Radar Echos						Infrared Temperatures		
	Polarized			Depolarized			Polarized			Depolarized					
	MEAN	σ	N	MEAN	σ	N	MEAN	σ	N	MEAN	σ	N	MEAN	σ	N
All Geologic map units	3.76	0.095	1059	3.35	0.23	1059	105	19	928	109	26	919	111	15	1061
Mare (unit Im)	3.75	0.078	429	3.24	0.17	429	100	15	407	97.3	19	401	118	18	429
Dark mare (unit Imd)	3.76	0.083	20	3.36	0.11	20	110	12	20	109	20	20	126	12	20
Young craters & slopes (units C--)	3.78	0.11	170	3.43[1] (3.50)	0.27	170[1] (126)	102[1] (102)	20	145[1] (141)	111[1] (118)	32	144[1] (100)	107[1] (105)	12	170[1] (126)
Eratosthenian-craters (units E--)	3.87	0.10	45	3.66	0.28	45	103	15	28	136	24	28	108	20	45
Eratosthenian-Imbrium craters (unit EI)	3.90	0.10	34	3.76	0.24	34	97	16	17	152	16	17	102	2	34
Cayley Fm. (units Ica, Icas, Icah)	3.74	0.070	35	3.39	0.10	35	114	22	35	121	26	35	104	5	35
All I units (except Cayley, mare)	3.76	0.12	237	3.37	0.23	237	117	21	190	119	25	188	104	6	237
All pre-Imbrium (units pI--)	3.76	0.11	114	3.43	0.23	114	107	16	94	122	24	94	103	4	116
Mare 79 (unit Im on LAC 79)	3.71	0.067	40	3.11	0.14	40	98	15	40	97	19	40	101	5	40
Mare 77 (unit Im on LAC 77)	3.72	0.018	5	3.76	0.024	5	--	--	--	--	--	--	101	2	5
Mare 76 (unit Im on LAC 76)	3.73	0.047	90	3.18	0.015	90	108	18	81	106	10	75	107	4	90
Mare 58 (unit Im on LAC 58)	3.72	0.023	16	2.99	0.066	16	73	17	10	103	11	10	108	4	16
Mare 57 (unit Im on LAC 57)	3.75	0.082	165	3.26[2] (3.24)	0.17	165[2] (138)	102	13	163	101[2] (97)	21	163[2] (136)	123[2] (118)	20	165[2] (151)
Mare 56 (unit Im on LAC 56)	3.78	0.094	113	3.32 (3.32)[2]	0.11	113 (96)[2]	93	11	113	86 (84)[2]	14	113 (96)[2]	127 (120)	18	113 (96)[2]
Cca (unit Cca on LAC 56)				3.24		44	102		44	96		44	113		44

1/ Mare-like unit Cca included. Number in parentheses is adjusted for young craters and bright slopes with unit Cca removed. Mean for unit Cca listed with mare units.

2/ Number in parentheses is for average with small Copernican craters and rays removed.

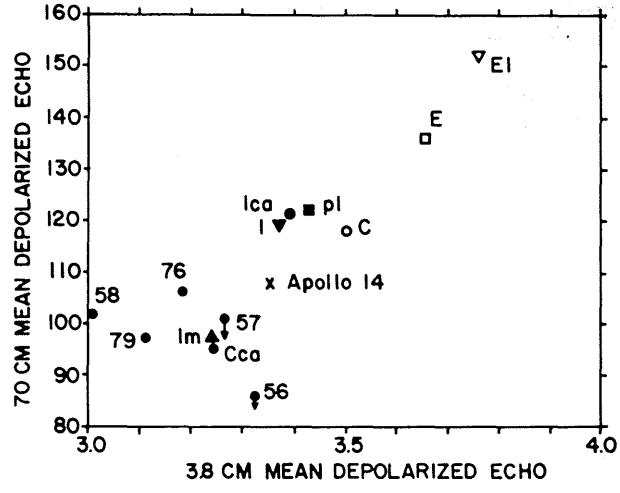

Figure 23. Averaged or mean 3.8 and 70 cm depolarized radar echoes for various geologic map units. Designators are: (1) Apollo 14--all geologic units, (2) C--Copernican craters and bright slope material, (3) E--Eratosthenian crater units, (4) EI--Eratosthenian-Imbrian crater units, (5) I--all Imbrian units except mare materials and Cayley Formation, (6) pI--all pre-Imbrian units, (7) Ica--Cayley Formation, (8) Im--mare material, (9) Cca--Cavalerius Formation, and (10) 56, 57, 58, 76, 77, and 79--mare materials in LAC charts 56, 57, 58, 76, 77, and 79. Arrows for mare material in LAC charts 56 and 57 indicate displacement of point after removal of anomalous values near Suess and Reiner A.

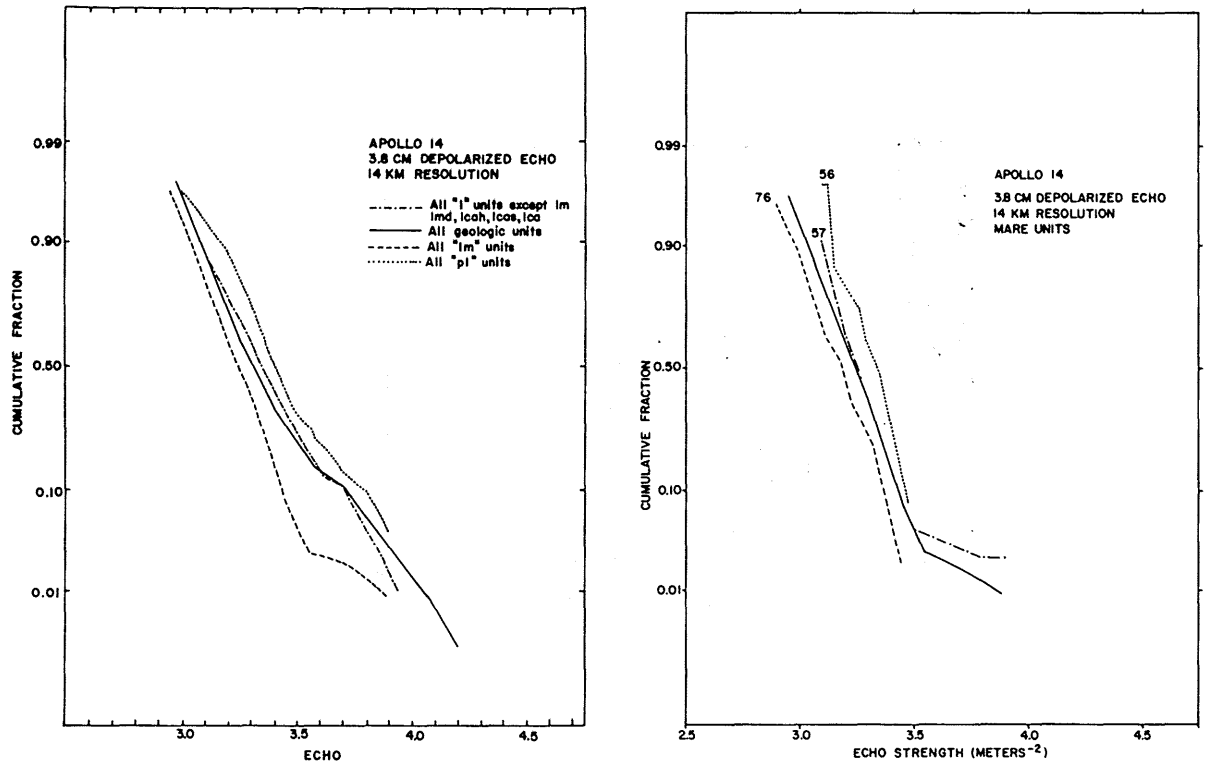

Figure 24. Frequency distributions of 3.8 cm depolarized radar echoes plotted on probability paper: (a) for all geologic units, all mare units (all Im), all Imbrian units (except Im, Imd, Icas, Icah, and Ica), and all pre-Imbrian units (all pI); and (b) for all mare materials (Im), mare material in LAC 56 (56), mare material in LAC 57 (57), and mare material in LAC 76 (76). Note tendency for linearity of distributions of all units except at large echoes where positive departures or "tails" occur. Note also overlap of echo strengths of the various units.

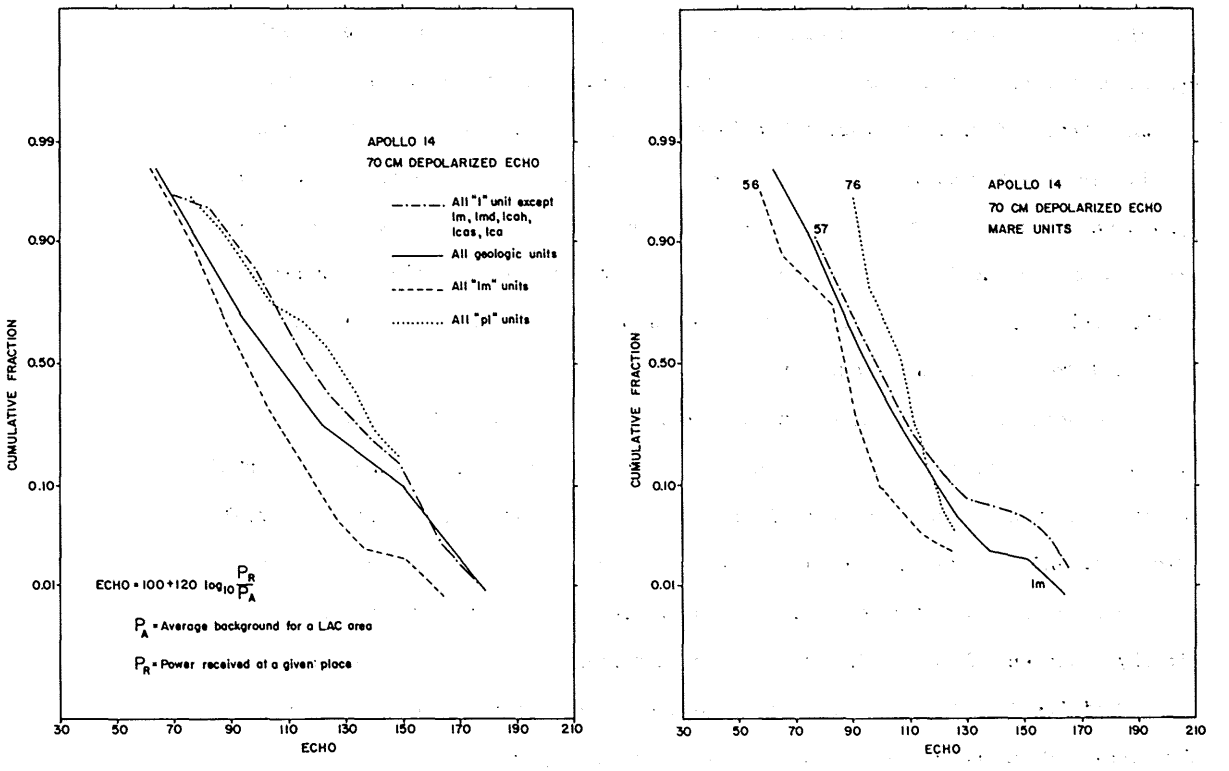

Figure 25. Frequency distributions of 70 cm depolarized radar echoes along Apollo 14 bistatic-radar ground track plotted on probability paper: (a) for all geologic units, all mare units (Im), all Imbrian units (except Im, Imd, Icas, Ica, and Icah); and all pre-Imbrian units (all pI); and (b) for all mare materials (Im), mare materials in LAC 56 (56), mare material in LAC 57 (57), and mare material in LAC 76 (76). Note tendency for linearity of some distributions, especially mare material. Some distributions have positive departures or "tails" at large values of echo strength. Note overlap of echo strengths of the various units.

table 2). A similar result is obtained for the positive departure in LAC 56. Here, the average mare depolarized echo is 84, but in the vicinity of Reiner A it is near 100.

E. Infrared eclipse temperatures and geologic map units

Scaled values of infrared eclipse temperatures yield, roughly, a two-fold division of the Moon: (1) western mare materials, and (2) eastern mare materials, upland units, and crater units. Averages of western mare materials in LAC 56, 57, unit Cca, and unit Imd (see table 3) are 118, 120, 114, and 126. The values are larger than the average of all geologic units (111). Eastern mare materials, upland units, and crater units are less than the average of all geologic units and are between 102 and 108. These results are similar to the bistatic-radar results in that only mare materials in the western maria (LAC 56 and 57) are clearly separated from upland and crater units.

Frequency distributions of infrared eclipse temperatures have some similarities with the radar echo distributions: (1) some of the distributions have marked positive departures from the general trend of the curve--especially mare materials (fig. 26), and (2) the distributions vary enough so that there is considerable overlap of values for each geologic map unit. The distribution curves are not clearly Gaussian, although the one for mare material in LAC 76 is an exception.

Positive departures (tails) for mare materials in LACs 56 and 57 are again the result of the Reiner A area with an average anomaly value of 165, compared to 120 for mare materials in LAC 56. The crater Suess plus its companion crater have an average anomaly value of 175, compared to 118 for the mare material in LAC 57. Removal of these high anomalous values from the distribution would eliminate or substantially reduce the "tails."

F. Areal correlation: Delisle-Diophantus area

Geologic units near Delisle and Diophantus are related to impact cratering, mare volcanism, and relicts of older units that have survived these two processes. Superposition relationships partly substantiate earlier work which indicated that impact cratering and mare formation occurred concurrently (Moore, 1965). These units, characterized by distinct topographies and albedos (fig. 14), are shown on the geologic sketch map (fig. 27 and table 4) where informal designations are used. The youngest units are bright halo craters (unit br). One of these is

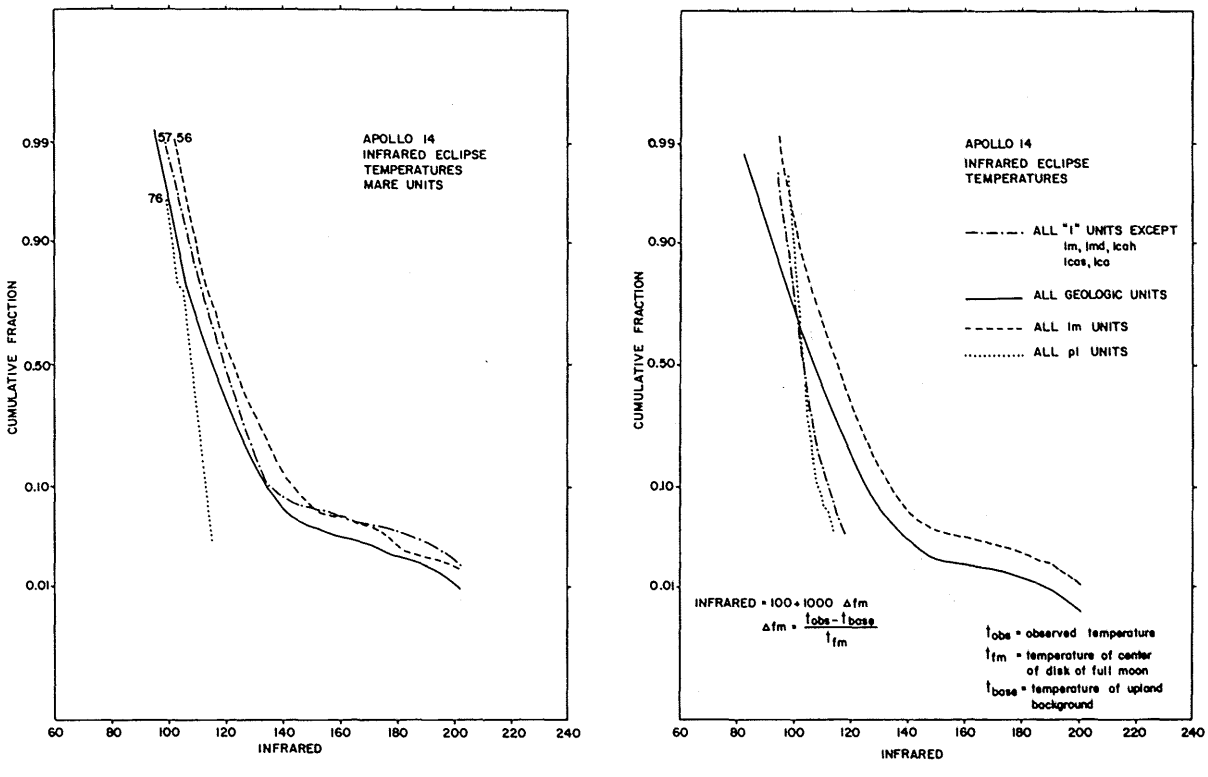

Figure 26. Frequency distributions of scaled infrared eclipse temperature along the Apollo 14 bistatic-radar ground track plotted on probability paper: (a) for all geologic units, all mare units (all Im), all Imbrian units (except Im, Imd, Icas, Icah, and Ica), and all pre-Imbrian units (all pI); and (b) for all mare materials, and mare materials in LAC 56 (56), LAC 57 (57), and LAC 76 (76). Note positive departures in distributions at large values for mare material (except 76).

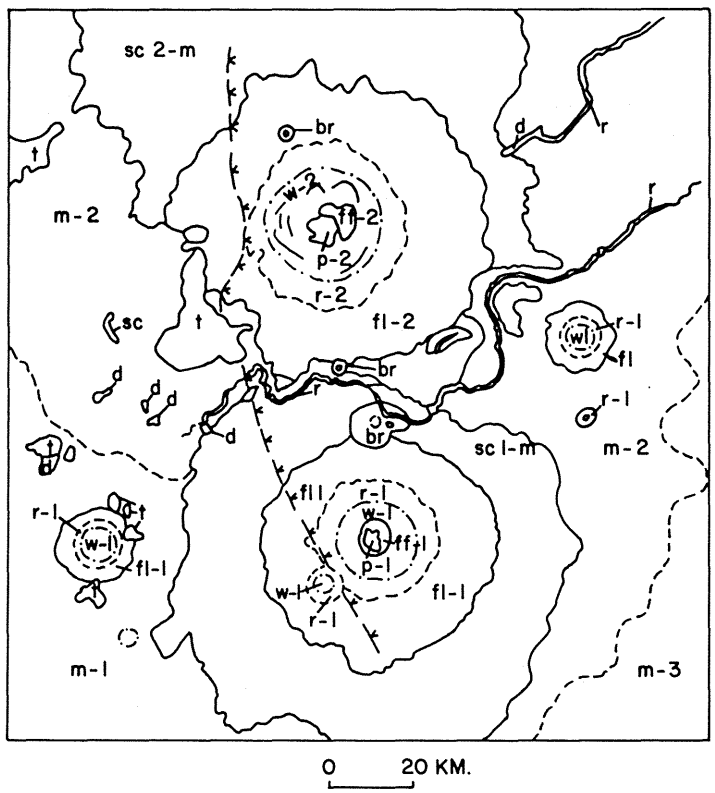

Figure 27. Geologic sketch map of the Delisle-Diophantus area of the Moon. Map unit designators are informal (see table 4).

Table 4. Informal geologic map units in the Delisle-Diophantus area and their characteristics

Geologic units in order of relative age	Unit Designator	Photogeologic characteristics	3.8 cm Depolarized Echo strength	70 cm Depolarized Echo Contour Value	Infrared Eclipse Temp. Contour Value	Color
Bright halo craters	br	Sharp, high rims, deep interior, surrounded by bright halo, and ejecta blocky	3.4-4.0	4-8	4+	red, strong
Craters, age group 1						
Central peak material	p-1	Steep slopes, high albedo, forms peaks	3.1-3.7	12-16+	4+	
Floor material	ff-1	Level surface, moderate albedo	3.1-3.7	12-16+	4+	
Wall material	w-1	Steep slopes, high albedo, rocks exposed	3.1-4.0	12-16+	4+	
Rim material	r-1	Moderate slopes, rough, moderate albedo, hummocky with concentric ridges	3.1-3.7	4-8	3-4	
Flank material	fl-1	Moderate slopes, rough, moderate albedo, radial, anastamosing, and chevron ridges	2.5-3.4	2-4	2-4+	
Secondary craters-mare	scl-m	Level surface, moderately rough, chains of craters	2.5-3.4	2-4	0-4+	
Mare material, young	m-1	Level surface, smooth, low albedo, bounded by flow scarps	< 2.5-3.1	2-3	2-3	blue, strong
Mare material	m-2	Level surface, smooth, low albedo, cratered	< 2.5-3.4	2-4	2-3	blue
Craters, age group 2						
Central peak material	p-2	Steep slopes, high albedo, forms peaks	2.8-3.4	6-8+	3-4+	
Floor material	ff-2	Level surface, moderate albedo	2.8-3.4	6-8+	3-4+	
Wall material	w-2	Steep slopes, high albedo, rocks exposed, slump terraces	2.8-4.0	6-8+	3-4+	
Rim material	r-2	Moderate slopes, rough, moderate albedo, hummocky with concentric ridges	2.5-3.4	4-8	2-3	
Flank material	fl-2	Moderate slopes, rough, moderate albedo, radial, anastomosing, and chevron ridges	< 2.5-3.4	2-4	1-3	
Secondary craters-mare	sc2-m	Level surface, moderately rough, chains of craters	< 2.5-3.4	2-4	2-3	
Mare material, old	m-3	Level surface, smooth, low albedo, cratered	2.5-3.4	2-4	2-3	reddish
Older terrain	t	Steep to moderate slopes, high albedo, forms isolated hills and mountains	< 2.5-3.1	2-3	2	red

superposed on the ejecta of Diophantus. Two other bright halo craters are superposed on mare material and ejecta from Delisle. Ejecta from Diophantus, Diophantus A, and Diophantus B (units r-1, fl-1, and scl-m) are superposed on mare material (units m-2 and m-1). Youngest mare material (unit m-3) is superposed as flow lobes on older mare material (unit m-2). The relationship between mare unit m-3 and Diophantus is not clear. Mare material (unit m-2) is superposed on ejecta from Delisle (fl-2). These two young mare materials (units m-3 and m-2) are relatively "blue" (Whitaker, 1973). The third mare material (unit m-1) is redder than the two previous mare units and appears to be older judging from the large number of craters on its surface.

Craters, domes, collapse depressions, and rilles (d, r) are features associated with mare volcanism. Isolated hills and mountains of older terrain (t) and some ejecta from impact craters were not entirely covered by mare material and protrude through it. A west-facing scarp crosses the area just west of Delisle and Diophantus in a north-south direction. Elevations of the rille are lower west of the scarp, higher in the region between Delisle and Diophantus and lower again to the east suggesting a broad arch. (LTO 39 B-1, B-2, Defense Mapping Agency, 1974).

Based on depolarized echo strength and eclipse temperatures, the geologic map units may be grouped into five categories as shown in table 5.

Table 5. Ranking of informal geologic map units by magnitude of response to terrestrial remote sensing data.

	3.8 cm depolarized echo strength	70 cm depolarized echo contour value	Infrared contour value
Largest values (5)	w-1, w-2, br	p-1, ff-1, w-1	br, p-1, ff-1, w-1
(4)	p-1, ff-1, r-1 ff-1	p-2, ff-2, w-2	r-1, p-2, ff-2, w-2
(3)	p-2, ff-2	br, r-1, r-2	fl-1 m-1, m-2, m-3
(2)	m-2, r-2, m-1, fl-2 scl-m, sc2-m	fl-1, scl-m, fl-2 sc2-m m-2, m-1, m-3	scl-m, r-2 fl-2, sc2-m
Lowest values (1)	m-3, t	t	t

If each of these units is given a weight from one to five in each remote sensing category as indicated and the results summed across categories, the units may be grouped as shown in table 6. These groupings show the following: (1) various units of a given crater fall into different groups, (2) the group number for corresponding units of the two craters increases from the crater outward, (3) group numbers of the younger Diophantus crater are lower than those of corresponding map unit of the older Delisle, (4) there is no clear correlation between relative age and position in the table, (5) units in groups III and IV are similar in properties, and (6) older terrain is distinctly low.

Table 6. Ranking of informal geologic map units using weighted magnitudes of response to terrestrial remote sensing data in Table 5.

Group	Small craters	Diophantus	Delisle	Mare units	Old terrain
I (14-15)		w-1 ff-1, p-1			
II (10-13)	br	r-1	w-2 p-2 ff-2		
III (7-9)		fl-1	r-2	m-2, m-1	
IV (4-6)		scl-m	fl-2 sc2-m	m-3	
V (3)					t

G. Intercorrelation of bistatic-radar and terrestrial remote sensing data

Comparison of the bistatic-radar results and terrestrial remote sensing data along the bistatic-radar ground track show: (1) strong direct correlation between average S-band rms slopes and average depolarized radar echoes for various map units, (2) a strong inverse correlation between average S-band rms slopes and average infrared eclipse temperatures, (3) weak correlation between infrared temperatures and depolarized radar echoes, (4) weak to non-existent correlation between VHF rms slopes and depolarized radar echoes, (5) a weak inverse correlation between VHF rms slopes and infrared anomalies, (6) a separation of geologic units into two groups: (a) western maria and (b) eastern maria, upland terrain, and crater units, and (7) a possible subset of mare units with inverse trends.

The strong direct correlation between averaged S-band rms slopes and averaged terrestrial radar depolarized echoes at 3.8 cm and 70 cm wavelengths for

the geologic units are shown in figure 28. Separation of mare materials (Im, digits, and Cca) from upland and crater units is quite clear for depolarized echoes at both wavelengths. There is also a direct linear relationship between the rms slopes and echoes when the maria are lumped together (i.e., Im in figure 28). Mare materials which appear smooth to the S-band radar have low echo strengths while the roughest units to the S-band radar have the largest average echoes. Individual mare units (digits in fig. 28) show an inverse linear trend when S-band rms slopes are compared with the 3.8 cm depolarized echoes. This correlation should be treated with caution, however, because it may be an unintentional result of the calibration procedures employed.

Comparison of average S-band rms slopes and infrared eclipse temperature anomalies show they are negatively correlated (fig. 29). In contrast with the comparisons above, only the mare materials in LACs 56 and 57 (56 and 57 in fig. 29) are clearly separated from the upland and crater units. Similar results are obtained when VHF rms slopes are compared with infrared eclipse temperature anomalies but scatter is larger and the correlation weaker (fig. 29).

Comparison of average depolarized radar echoes with average infrared eclipse temperatures reveals a weak negative correlation between them (fig. 30). This correlation appears a little stronger for the 70 cm echoes and infrared temperatures. For both comparisons, mare materials in LAC 56 and 57 are well separated from upland and crater units whereas the others are not.

Comparison of average VHF rms slopes with average depolarized radar echoes does not have the strong direct correlation as the S-band rms slopes (fig. 31). Mare materials (Im) tend to have small echo strengths and small rms slopes, the exception being mare material in LAC 79. Echo strengths for upland and crater units seem to be independent of VHF rms slopes. Here, as in the case for S-band rms slopes, mare materials are separated from upland and crater units.

Detailed correlations and lack of correlations between the bistatic-radar results and terrestrial remote sensing results exist. A lack of correlation is found in LAC 57 near the crater Suess and its small bright companion ($\approx$ 47.5° W., 2.0° N.) where the bistatic-radar reveals little or no change in surface roughness. In contrast, very large infrared anomalies and large depolarized echoes occur here. A similar result is found near Reiner A in LAC 56 ($\approx$ 51.5° W., 3.0° N.).

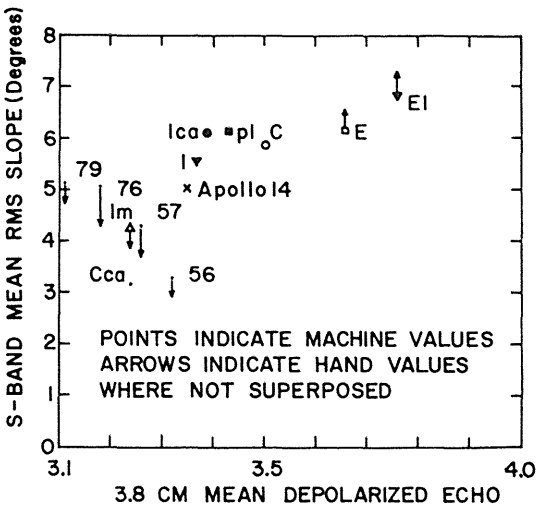

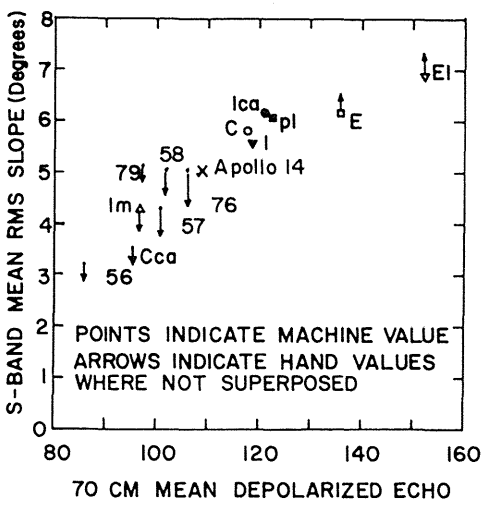

Figure 28. Averaged S-band rms slopes and averaged terrestrial depolarized radar echoes for various geologic map units: (a) average 3.8 cm depolarized echoes and rms slopes (data points for mare material in LAC 58 not shown), and (b) average 70 cm depolarized echoes and rms slopes. Note positive correlation between S-band, rms slopes, and depolarized echoes. Mare materials in various LAC charts (56, 57, 76, and 79) form subset for which 3.8 cm depolarized echo is negatively correlated with S-band rms slopes. Note separation of mare material (Im, Cca, and digits) from upland and crater units (I, pI, Ica, C, E, EI).

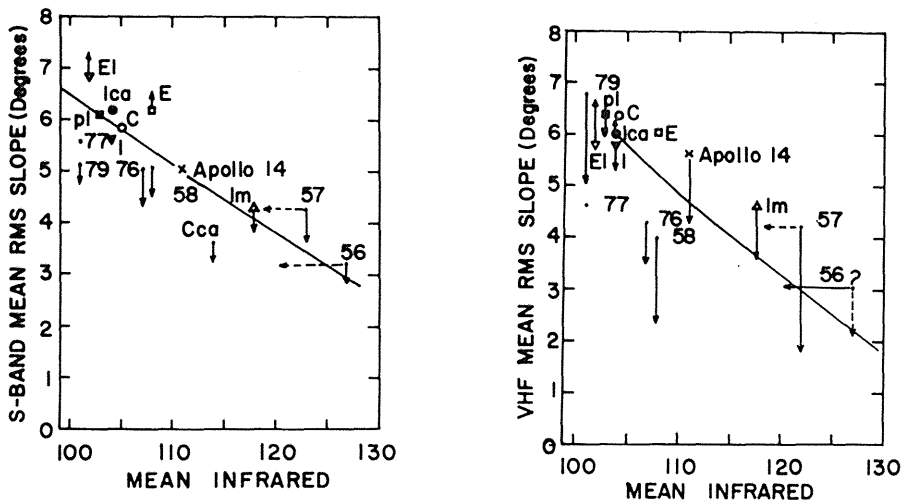

Figure 29. Averaged S-band and VHF rms slopes and averaged infrared eclipse temperature anomalies for various geologic map units. Note negative slope to data. Mare material in LACs 56 and 57 and unit Cca are separated from upland and crater units whereas other mare units are not separated. Points indicate machine values; vertical arrows indicate hand values where not superposed; horizontal arrows for mare material in LAC 56 and 57 indicate displacement of point after anomalous values near Suess and Reiner A are removed.

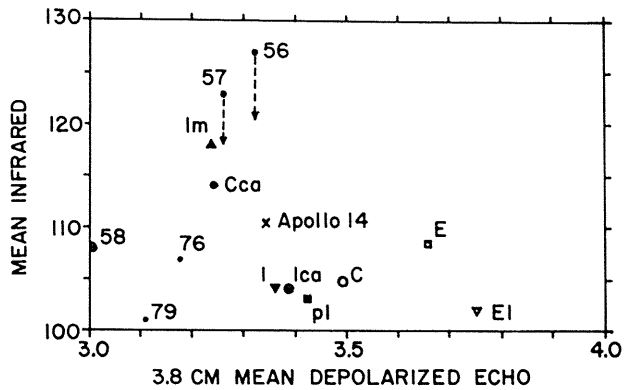

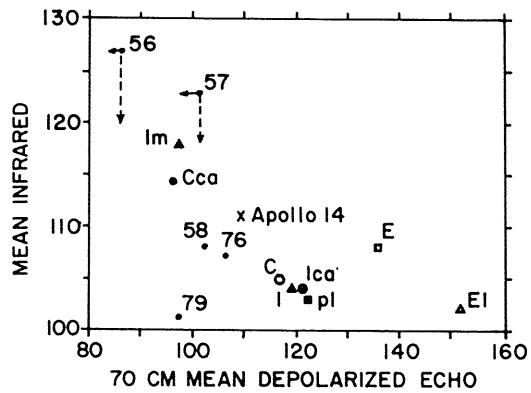

Figure 30. Averaged infrared eclipse temperature values and averaged terrestrial depolarized radar echoes for various geologic map units: (a) average 3.8 cm depolarized echoes and infrared anomalies, and (b) average 70 cm depolarized echoes and infrared anomalies. Note negative correlation for mare materials. Mare materials in LAC 56 and 58 are the only mare materials clearly separated from crater and upland units. Arrows indicate displacement of values for mare material in LAC 56 and 57 after removal of anomalous values near Suess and Reiner A.

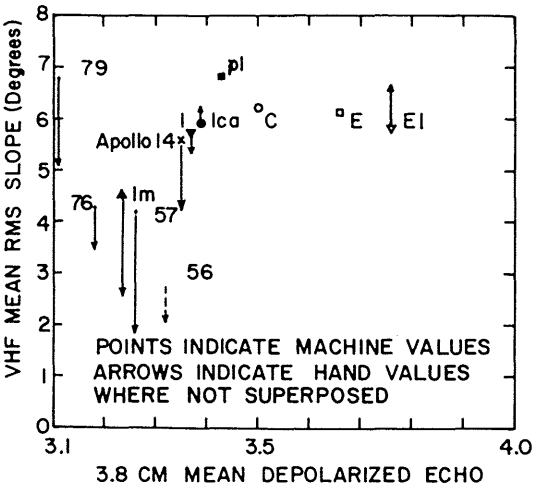

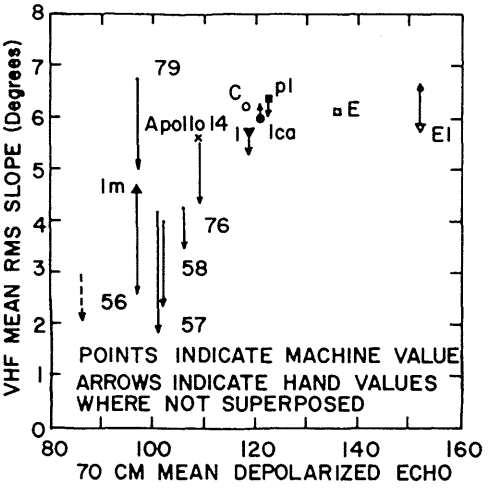

Figure 31. Averaged VHF rms slopes and averaged terrestrial depolarized radar echoes for various geologic map units: (a) average 3.8 cm depolarized echoes and rms slopes (data point for mare material in LAC 58 is not shown), (b) average 70 cm depolarized echoes and rms slopes. Note lack of correlation between rms slopes and echoes.

As noted previously, these features produce the "tails" to the frequency distributions of infrared anomalies and radar echoes. Another lack of correlation is illustrated by the frequency distributions for mare material in LAC 57 where the bistatic-radar indicates a two-fold division of the mare material (figs. 19 and 20) but there is no clear evidence for this in the terrestrial remote sensing frequency distributions (figs. 24, 25, and 26).

H. Correlation between relative ages and rms slopes

Relative ages correlate in a very general way with both S-band and VHF hand calculated rms slopes (table 7). For upland units with D_L values larger than 500 m, S-band and VHF rms slopes are nearly constant at about 5.5° whereas mare units are typically less. In detail, correlation between relative ages (D_L values) and S-band rms slopes does not appear particularly good (fig. 32), but the correlation with VHF rms slopes is better. The Fra Mauro Formation is an exception to this, however, because VHF rms slopes of the Fra Mauro Formation are comparable to those of the Cayley-type plains. The S-band radar values contributing to the poor correlation with relative age occur in LAC 57 (fig. 3, west) where the radar specular points cross a variety of terrain that includes uplands, remnants of crater rims, and the older mare of the Maestlin region. If data from this region for both S-band and VHF are excluded, correlation with relative age for the VHF rms slopes remains the same and relative age and S-band rms slopes also correlate (see table 7, fig. 32, 40° W.).

I. Regolith thickness correlations

Regolith thickness for a variety of map units near the Apollo 14 bistatic-radar track was estimated using Lunar Orbiter images with a nominal 1.0 m resolution. It was necessary to use images with nearly constant resolutions because resolution affects the magnitude of the estimate of regolith thickness using the crater morphology technique (fig. 33, table 3). This was tacitly demonstrated by the original work (Oberbeck and Quaide, 1967; Quaide and Oberbeck, 1968). An average thickness of 8-9 m was estimated for the region near Flamsteed using Lunar Orbiter moderate resolution photographs with 8.2 m resolution. For the same general area, a median (and average) thickness of 3-4 m was estimated using Lunar Orbiter III high resolution photographs with 1.2 m resolution. Resolution dependence of the method is further substantiated by data from Hipparchus. Estimates

Table 7. Relative ages and hand calculated rms slopes of various areas along the Apollo 14 bistatic radar track.

Nearest coord. Along track	D_L (m)	RMS slope VHF	RMS slope S-band	Frame Number	Description
-12°, 51°	~ 250	2.0	--	V-44m	Mare Fecunditatis
-12°, 47°	235±35	2.0	--	V-44m	Mare Fecunditatis
-11°, 36°	~ 400	4.2	4.2	II-5, 12, 20,32 III-5,11,19,60 V-74	N. Mare Nectaris
-11°, 15°	550±50	5.2	5.2	AS-16-M-0164	Cayley plain
- 8°, 14°	540±90	5.8	5.7	AS-16-M-0165	Cayley in floor Dolland B
- 8°, 11°	600±120	5.8	5.5	AS-16-M-0165	Cayley plain
- 8°, 6°	510±50	5.5	5.5	V-98m	Cayley in floor Hipparchus
- 7°,-13°	310±50	4.7	5.0	II-138m	Northern Mare Nubium
- 3°,-17°	1000+	5.2	5.4	AS-16-M01676	Fra Mauro Formation
- 2°,-18.7°	355±65	4.3	4.5	III 131m	Oceanus Procellarum East of Lansberg
- 2°,-20°	260±10	3.6	4.2	III 124m	same
- 1°,-22.5°	215±15	3.0	4.0	III 145m	same
0°,-24°	220±10	2.1	3.8	V-149m	same
0°,-34°	145±25	2.0	4.8	II-191m	Oceanus Procellarum West of Lansberg
1°,-34.3°	150±5	2.0	4.0	II-179m	same
1°,-34.5°	150±20	1.9	4.7	I-156m	same
2°, 36°	170±20	2.2	4.8	I-156m	same
2°,36.3°	195±25	2.0	3.0	I-153m	same
3°,41.5°	170±15	2.0	3.5	III-170m	Oceanus Procellarum Southwest of Maestlin
3°,41.7°	215±15	1.9	3.0	III-170m	same
3°, 42	235±55	2.0	2.8	III-163m	same
4°, 43	205±25	2.1	3.3	III-204m	same

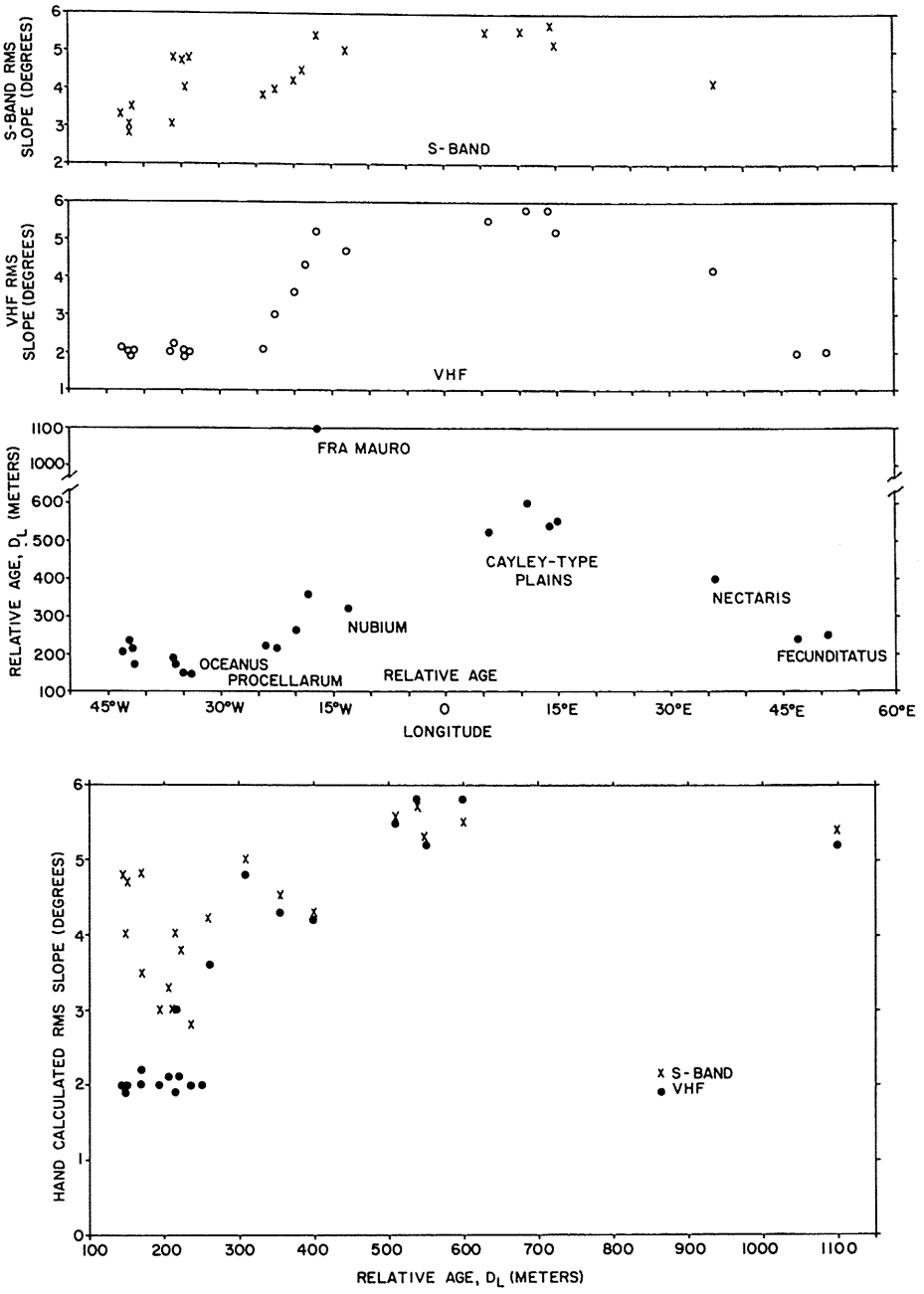

Figure 32. Bistatic-radar rms slopes and relative ages of units near the Apollo 14 ground track. Note general correlation between relative age, S-band rms slopes, and VHF rms slopes.

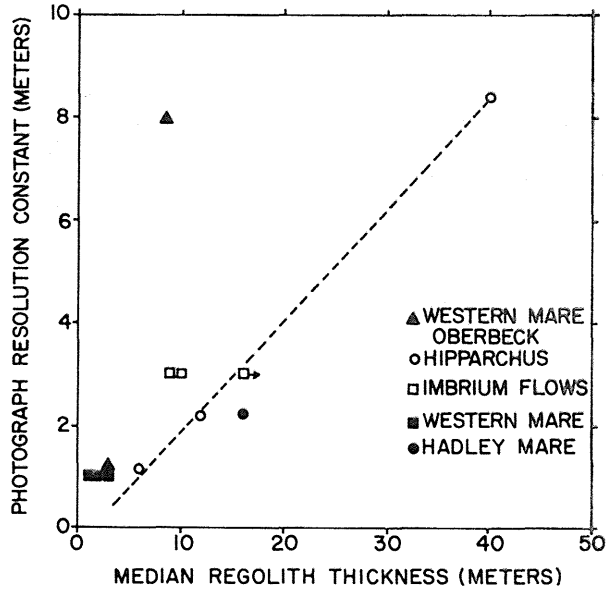

Figure 33. Comparison between regolith thickness estimates and photographic resolution. Open circles--Hipparchus, filled circle--Hipparchus (Oberbeck and Quaide, 1968), filled triangles--Oceanus Procellarum in and near Flamsteed (Oberbeck and Quaide, 1967; Quaide and Oberbeck, 1968), filled squares--maria from Lunar Orbiter II and III high resolution (1.0 m) photographs, and open squares--Imbrium flows from Apollo panoramic photographs.

of regolith thickness for Hipparchus are 8 m, 10 m, and 40 m using Lunar Orbiter III high (1.2 m resolution), Lunar Orbiter V high (2.2 m resolution), and Lunar Orbiter III moderate (8.4 m resolution) photographs respectively. If photographs with similar resolutions are used, estimates of relative apparent thicknesses are possible.

Most of the areas sampled were mare material (unit Im) but some were upland materials (units Ica and Ifm). Estimated thicknesses were generally small for the mare units and larger for the upland units (table 8).

Estimated regolith thicknesses correlate with relative ages (D_L values) of the surfaces (fig. 34) in a general way. The chief exception is the Apollo 14 landing site (Fra Mauro). A thin regolith would not be predicted for Apollo 14. Rather, a rough linear extrapolation (Soderblom and Lebofsky, 1972, p. 292) of results plotted in figure 34 indicates the median regolith thickness should be 22 m or so. A large median regolith thickness (between 10 to 36 m; Moore, unpub. data) has been estimated. Radar data yield the same result (Tyler, 1968). Approximate extrapolation of Shoemaker's equations (Shoemaker and others, 1969, p. 100-101), using 790 m as the diameter where the steady-state cumulative frequency distribution joins the production cumulative frequency distribution (Boyce and others, 1974), places the maximum regolith thickness near 200 m, the minimum near 20, and the median near 35 m. Such large thicknesses are entirely consistent with visual impressions of the imagery of the Apollo 14 site that show degraded, subdued, and filled craters more than 500 m across (regolith > 50 - 100 m). South Triplet, some 90 m across, has a central mound suggesting some 18 m of regolith. Low estimates of regolith thicknesses near 8 m (Offield, 1970), 8.5 m (Kovach and others, 1971), and 5.6 - 9 m (table 8) are puzzling. Low estimates using crater morphologies and blocks around craters could result from incomplete sampling by crater size so that only the lower part of the probability distribution of thicknesses is sampled. The Active Seismic geophone array overlies the rims of two subdued craters (Swann and others, 1970, p. 46, fig. 3-13). The Active Seismic datum that is in better agreement with the filled craters at the site is the 229 m/sec layer that extends 46.5 to 84.5 m below the surface.

Our limited data on regolith thicknesses that can be correlated with remote sensing data suggest (fig. 35): (1) a negative correlation between regolith

Table 8. Lunar regolith thickness estimates and other remote sensing data for selected lunar areas

Location	Site, Photos	Unit Design.	LAC-Unit	Resolution	Albedo	Thickness (meters)	D_L (Ave) (meters)	70 cm dp	3.8 cm dp	IR	Machine S-band	Machine VHF	Hand calc. S-band	Hand calc. VHF
Central Oceanus Procellarum 2°N.,34° W.	LOII P12 187-3	Pm	57-Im	0.99m	93	1	145	103	1868	123	4.81	4.65	4.15	2.32
	187-189		57-Im	0.99m	93	3	145	103	1868					
Central Oceanus Procellarum 2° N.,43° W.	LOII P13a 198-199	Pm	57-Im	1.04m	82	1.5	205	80	1441	119	4.20	3.25	4.78	1.63
SE Oceanus Procellarum 1° S.,20° W.	LOIII P8 125	Ipm	76-Im	0.99m	102	5.5	255	109	1705	110	4.79	3.89	4.34	3.31
	127	Ipm	Im	0.99m	102	6	255	109	1705	110				
	131	If?	If	0.99m	116	9	355	110	1026	104	5.61	5.45	5.03	5.01
S. Central Oceanus Procellarum 3° S., 37° W.	LOIII P11	Pm	75-Im	1.16m	82	1.5	195	116	1535	115	3.26	--	1.55	--
Hipparchus 5° S.,4° E.	LOIII S17 108-111	Ica	77-Ica	1.1 m	138	6	510	139	2673	108	6.67	6.26	5.82	5.14
	LOV 24, 99	Ica		2.18m	138	12	570	139	2673	108	6.67	6.26	5.82	5.14
Hadley 25° N.,3° E.	LOV 26.1 105 106	Elm	41-Im	2.95m	111	10	230	94	1905	94	4.4	4.3	3.23	3.22
		IpIh	--	--	--	9		--	--	--	--	--	--	--
		pIm	Ifh	--	122	> 16	--	120	4273	102	5.60	6.51	4.67	6.20
Fra Mauro 17° S.,3.5° W.	LOIII S23 132-135	Is	76	1.22m	--	5.6	--	--	--	104				
		If	If	--	116	8	1000+	110	--	104				
		(Ifh)				6.7								
		(Ifr)				8								
Mare Imbrium 25° N.,25° W.	AXV Rec Pan 0260-0274	Phase III	40	≈ 3-4m	--	8	160	--	--	--	--	--	--	--
		Phase I-II			--	10	200	--	--	--	--	--	--	--
		No flows			--	5	250	--	--	--	--	--	--	--
Mare Serenitatis	AXV Rec Pan													
18° N.,26° E.	9558-9566	UNIT I,SE*	42-Im	≈ 3-4m	87	13	330	61	902	111	3.64		2.41	2.46
20° N.,26° E.	9558-9566	" IV,SE	42-Im		92	13	280	84	1514	112	3.67	3.41	2.28	1.75
25° N.,20° E.	9308-9322	" IV,EMS	42-Im		--	10	275	--	--	--	--	--	--	--
25° N.,13° E.	9336-9358	" II,W	42-Im		93	9	175	85	4502	120	4.28	4.58	3.28	3.30
17° N.,22° E.	9358-9566	Ibp,EId	42-Im		87	13	350	61	902	111	3.64		2.41	2.46
23° N.,29° E.	9560-9562	Unit I EI,NE	42-Im		--	15	205	--	--	--	--	--	--	--

For unit designations see: Howard, K. A., Carr, M. H., and Muehlberger, W. R., 1973, Basalt stratigraphy of southern Mare Serenitatis, Chapt. 29 of Apollo 17 Preliminary Science Report: Natl. Aeronaut. and Space Admin. Spec. Pub. NASA SP-330, p. 29(1)-29(25).
Thompson, T. W., Howard, K. A., Shorthill, R. W., Tyler, G. L., Zisk, S. H., Whitaker, E. A., Schaber, G. G., and Moore, H. J., 1973, Remote sensing of Mare Serenitatis, Chapt. 33 of Apollo 17 Preliminary Science Report: Natl. Aeronaut. and Space Admin. Spec. Pub. NASA SP-330, p. 33(3)-33(17).

3.8 cm depolarized echos, here, are not expressed in $\log_{10}$ form.

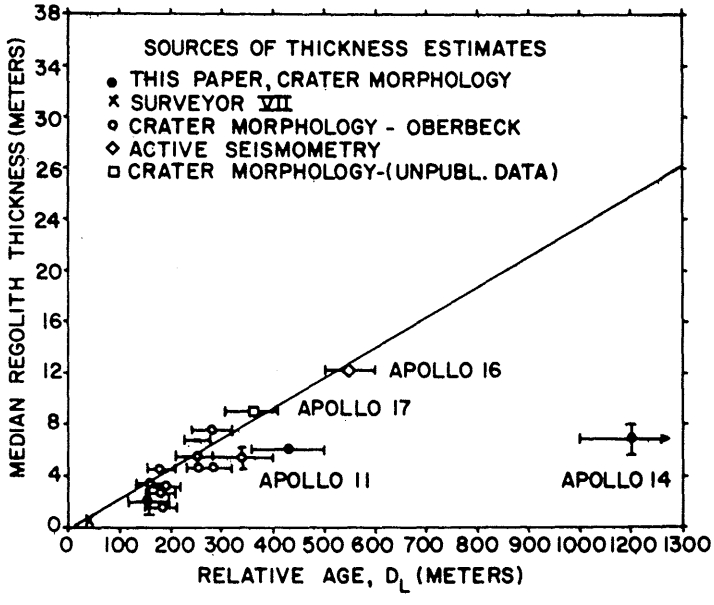

Figure 34. Correlation between regolith thickness and relative age of surface.

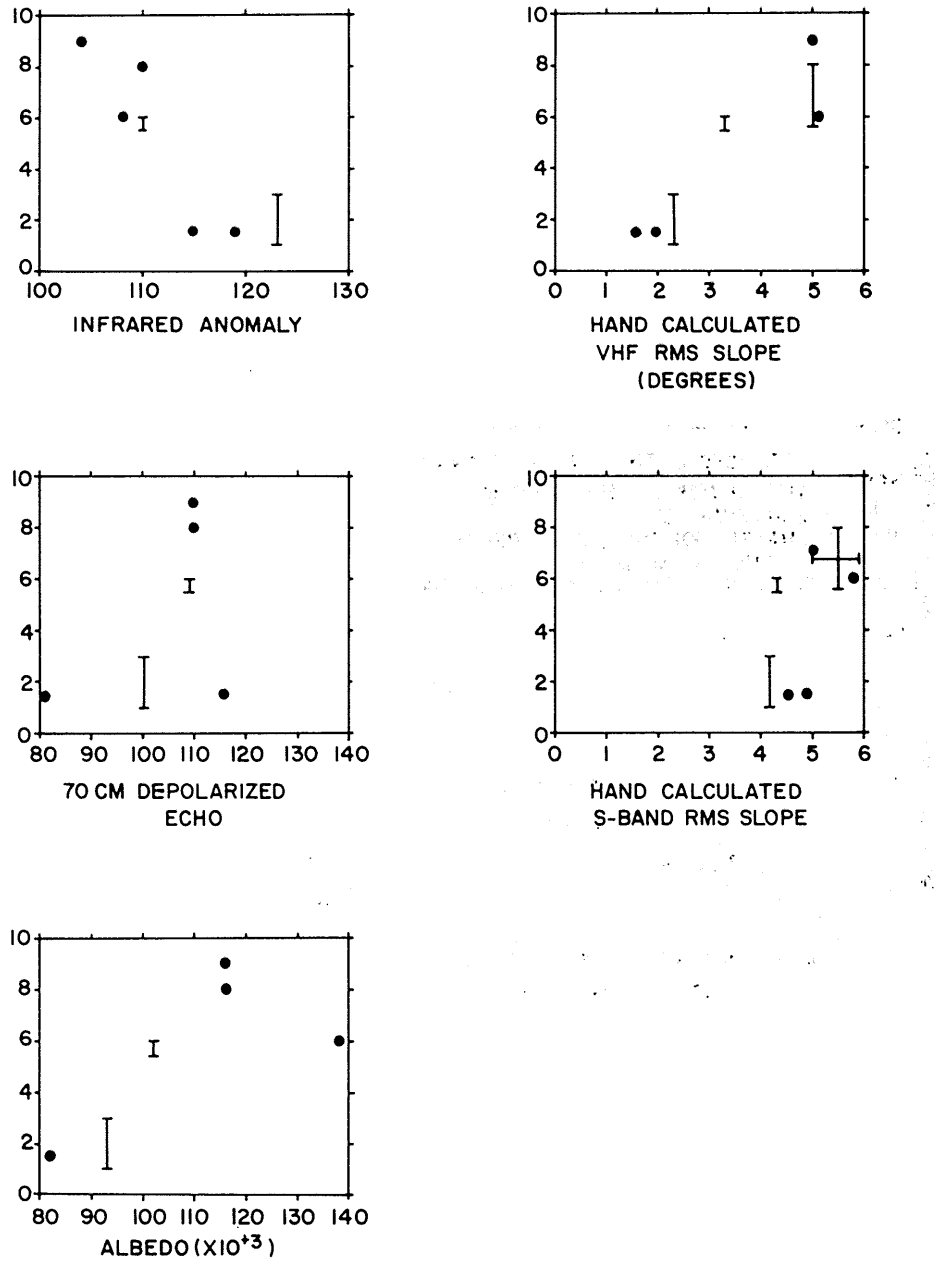

Figure 35. Comparison between regolith thickness and remote sensing data.

thickness and infrared anomaly temperature, (2) no correlation with 70 cm depolarized echoes, (3) a positive correlation between regolith thickness and VHF rms slope, and (4) a possible positive correlation between regolith thickness and S-band rms slopes. Crater units are excluded in this correlation.

J. Correlation between photogrammetric data for the Moon, experimentally cratered surfaces, and bistatic-radar results

Surfaces sampled using photography taken by the Lunar Topographic Camera and photogrammetry may be classified into three intergradational types using slope frequency distributions and relative magnitude of statistical parameters as a function of slope length. Further subdivisions are indicated by the magnitude of the statistical parameters at given slope lengths. The first type of surface, compared to a Gaussian distribution, has a larger frequency of large slopes, and a smaller frequency of small slopes (figs. 36 and 37; Moore and Tyler, 1974). This surface, typical of cratered plains units, is also characterized by a rather strong linear relationship between the logarithm of a statistical parameter for slope distributions (i.e., algebraic standard deviation, mean absolute slope, and median absolute slope) and the logarithm of slope length (figs. 36 and 37). Slope frequency distributions of the second type of surface are nearly Gaussian (figs. 38 and 39). The second type is also characterized by a less steep or even a convex upward relationship between the logarithm of the statistical parameter and the inverse of the logarithm of slope length (figs. 38 and 39). The third type has slope frequency distributions with frequencies of large slopes less than a Gaussian distribution and frequencies of small slopes larger than a Gaussian distribution (figs. 40 and 41). The log-log comparison of the statistical parameters and slope length is flat, except for large slope lengths (figs. 40 and 41). As with all natural surfaces, these types are gradational with one another.

Further subdivisions may be made on the basis of the magnitude of the statistical parameters within the three types. For the first type of surface, the algebraic standard deviation, mean absolute slope, and median absolute slope of the mare surface in Flamsteed (fig. 36) are smaller at given slope lengths than the Cayley surface sampled (fig. 37). Similar subdivision for the surfaces with Gaussian distributions may be made because the statistical parameters of the Theophilus flank sample are consistently smaller than those of the rim (compare figs.

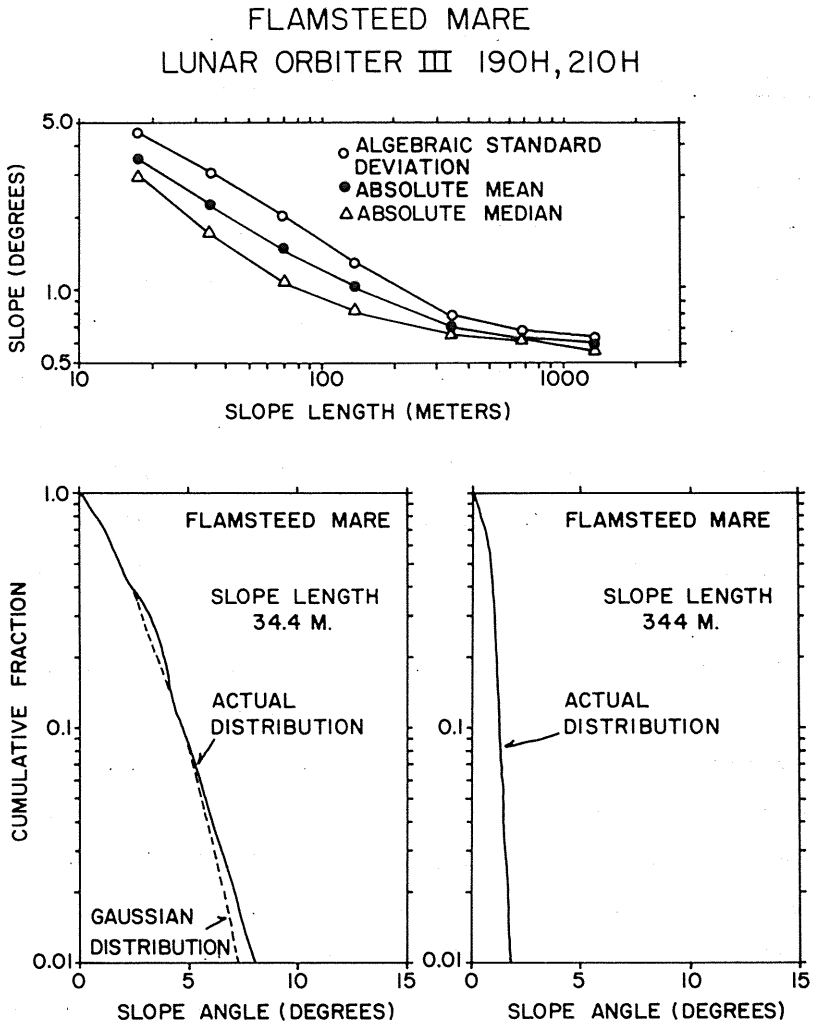

Figure 36. Variation of algebraic standard deviation, absolute mean, and absolute median with slope length and slope frequency distributions for smooth mare within the Flamsteed ring. (a) Algebraic standard deviation, mean absolute slope, and median absolute slope as a function of slope length. Note steep negative slope of curves at slope length between 17 and 344 m. (b) Slope frequency distribution at a slope length of 34.4 m (solid line); dashed line represents expectation for Gaussian distribution with same algebraic standard deviation of solid curve. Solid curve has larger frequency of slopes at large slope angles than Gaussian curve. (c) Slope frequency distribution at a slope length of 344 m. Surface is much smoother at large slope length than at small slope length. Data collected by Raymond Jordan using photogrammetric techniques and Lunar Orbiter III imagery (Lunar Orbiter III high resolution frames 190 and 210).

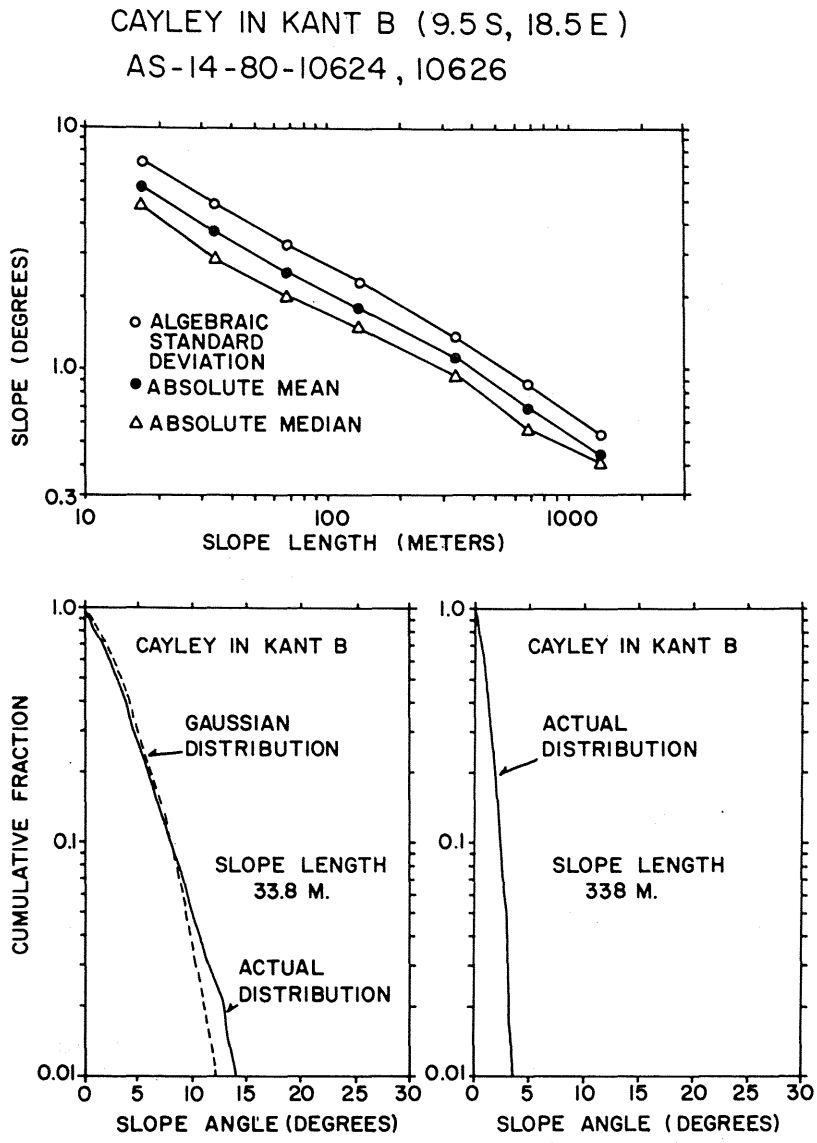

Figure 37. Variation of algebraic standard deviation, absolute mean, and absolute median with slope length and slope frequency distributions for cratered plain of Cayley Formation in Kant B (9.5° S., 18.5° E.). (a) Algebraic standard deviation, mean absolute slope, and median absolute slope as a function of slope length. Note steep negative slope of curves. (b) Slope frequency distribution at a slope length of 33.8 m (solid line); dashed line represents expectations for Gaussian distribution with same algebraic standard deviation as solid curve. Solid line has smaller frequency of slopes than Gaussian curve at smaller slope angles and larger ones at large slope angles. (c) Slopes frequency distribution at slope length of 338 m. Surface is much smoother at large slope length than at small slope length. Data collected by Raymond Jordon using photogrammetric techniques (Apollo 14 photographs AS-14-80-10624, 10626).

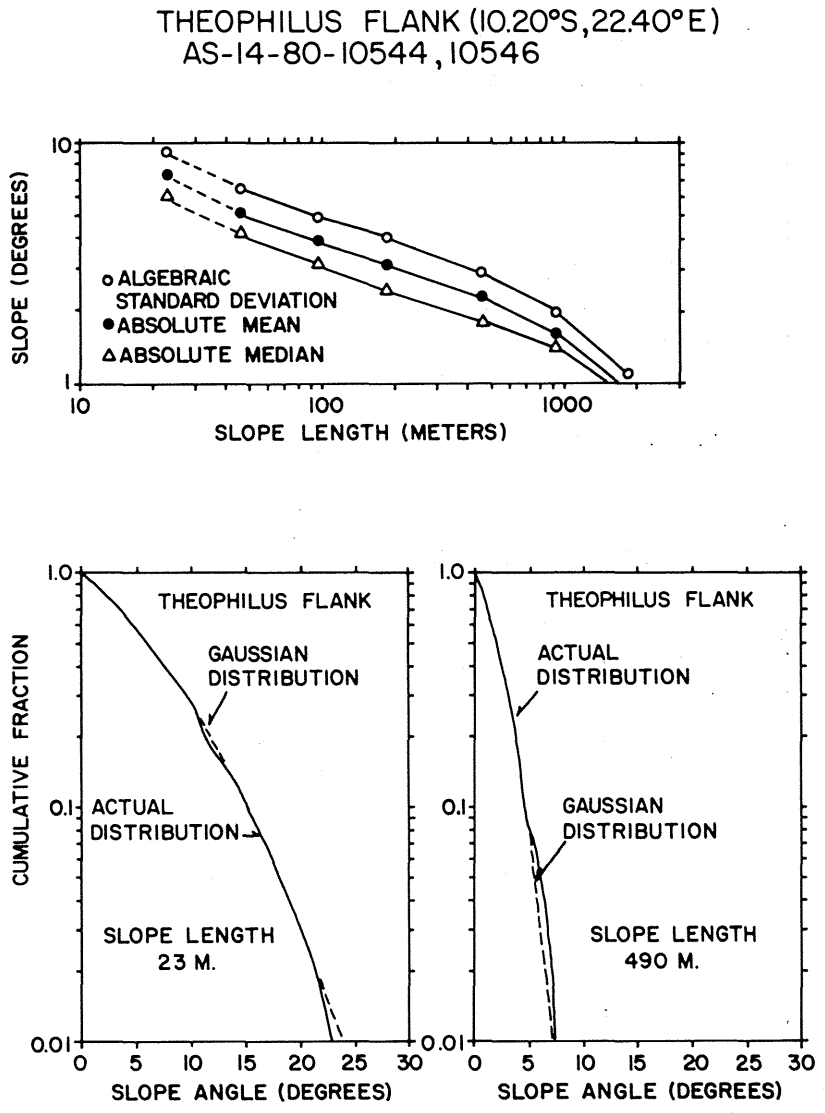

Figure 38. Variation of algebraic standard deviation, absolute mean, and absolute median with slope length and slope frequency distributions for the flank of Theophilus (10.2° S., 22.4° E.). (a) Algebraic standard deviation, mean absolute slope, and median absolute slope as a function of slope length. Note slope of curve is flatter than those in figures 36 and 37. Dashed lines indicate curves corrected for photogrammetric reading error. (b) Slope frequency distribution at a slope length of 23 m (solid line); dashed line represents expectations for Gaussian distribution with same algebraic standard deviation as solid curve. Solid curve is, for all practical purposes, Gaussian. (c) Slope frequency distribution at a slope length of 490 m. Solid curve is still essentially normal. Data collected by Raymond Jordan using photogrammetric techniques (Apollo 14 photographs AS-14-80-10544, 10546).

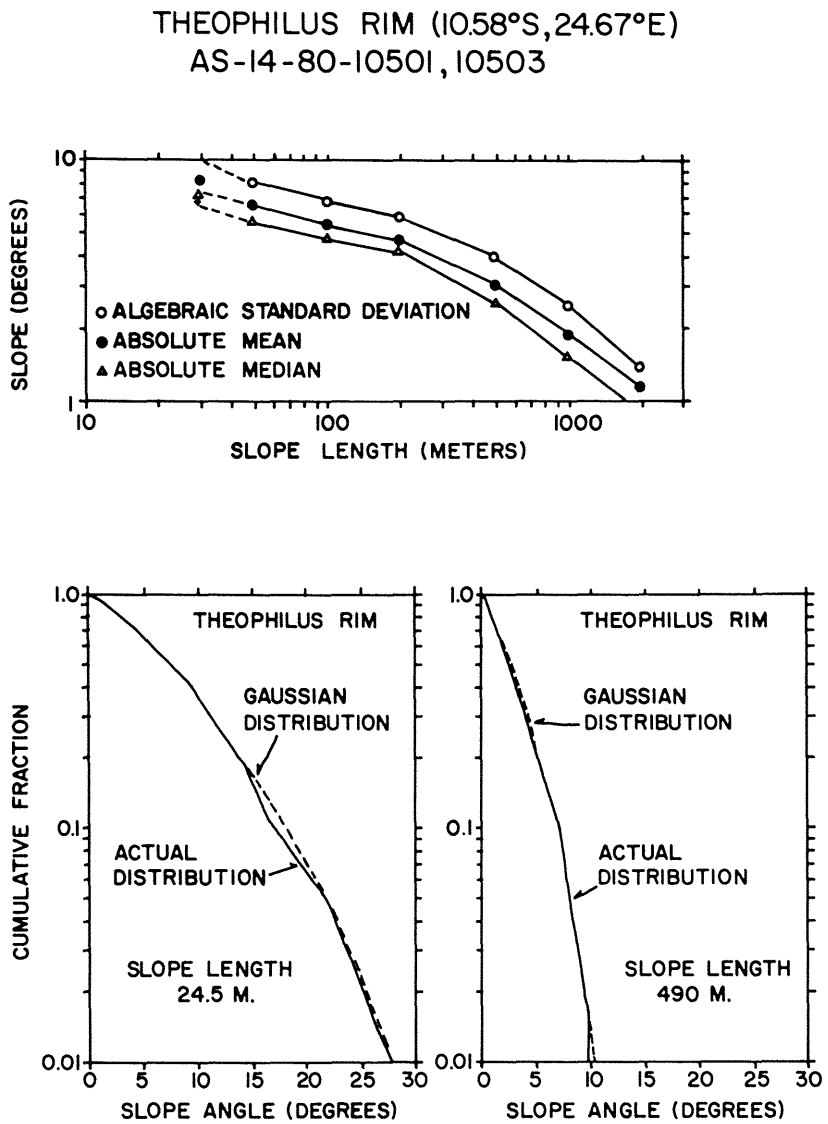

Figure 39. Variation of algebraic standard deviation, absolute mean, and absolute median with slope length and slope frequency distributions for the rim of Theophilus (10.58° S., 24.67° E.). (a) Algebraic standard deviation, mean absolute slope, and median absolute slope as a function of slope length. Slope of curve at small slope lengths is flatter than those in figures 36 and 37 and has arcuate form at largest slope lengths. Arrows and dashed lines indicate correction required for photogrammetric reading error. (b) Slope frequency distribution at a slope length of 24.5 m (solid line); dashed line represents expectations for Gaussian distribution with same algebraic standard deviation of solid curves. (c) Slope frequency distribution at a slope length of 490 m. Surface is smoother than at 24.5 m slope length and distribution is Gaussian. Data collected by Raymond Jordan using photogrammetric techniques (Apollo 14 photographs AS-14-80-10501, 10503).

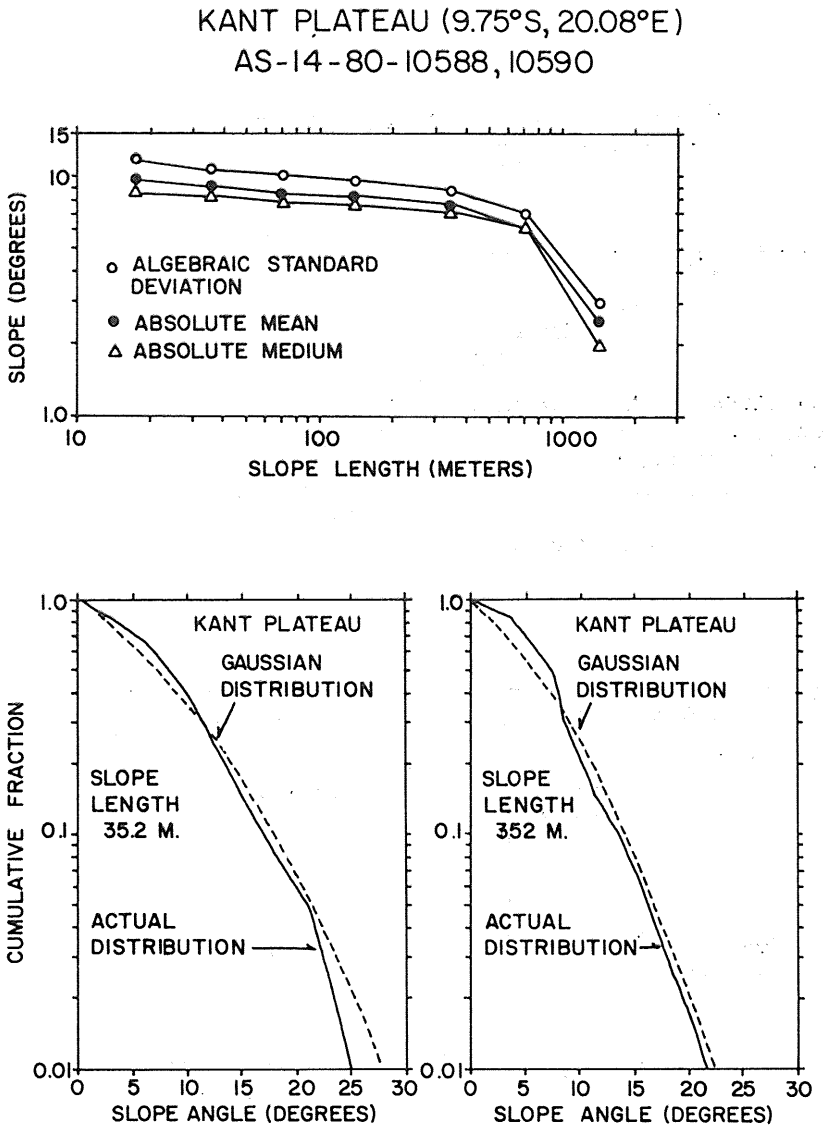

Figure 40. Variation of algebraic standard deviation, absolute mean, and absolute median with slope length and slope frequency distributions for Kant plateau (9.75° S., 20.08° E.). (a) Algebraic standard deviation, mean absolute slope, and median absolute slope as a function of slope length. Note flat curve for slope lengths less than 400 m. (b) Slope frequency distribution at a slope length of 35.2 m (solid line); dashed line represents expectations for Gaussian distribution with same algebraic standard deviation of solid curve. Frequencies of slopes are larger than Gaussian curve at small slope angles and smaller at large slope angles. (c) Slope frequency distribution at slope length of 352 m (solid line). Solid curve has similar properties as b and shows surface is smoother at larger slope length. Data collected by Raymond Jordan using photogrammetric techniques (Apollo 14 photographs AS-14-80-10588, 10590).